

Surface velocities in the hinterland of the Neumayer III station (Antarctica) derived from SAR-Interferometry

Niklas Neckel



UNIVERSITÄT HEIDELBERG
FAKULTÄT FÜR CHEMIE UND GEOWISSENSCHAFTEN
GEOGRAPHISCHES INSTITUT

DIPLOMARBEIT/DIPLOMA THESIS

Surface velocities in the hinterland of
the Neumayer III station (Antarctica)
derived from SAR-Interferometry

Author:

Niklas NECKEL
Herkenkrug 20
22359 Hamburg

Supervisor:

Dipl.-Phys. Reinhard DREWS
Dr. Wolfgang RACK

Referee:

Prof. Dr. Lucas MENZEL
PD Dr. Olaf EISEN

December 21, 2010

“Ich versichere, dass ich die beiliegende Diplomarbeit ohne Hilfe Dritter und ohne Benutzung anderer als der angegebenen Quellen und Hilfsmittel angefertigt und die den benutzten Quellen wörtlich oder inhaltlich entnommenen Stellen als solche kenntlich gemacht habe. Diese Arbeit hat in gleicher oder ähnlicher Form noch keiner Prüfungsbehörde vorgelegen.”

Heidelberg, den 21.12.2010 _____

Abstract

Surface velocities of polar ice are an important input parameter for mass flux calculations and ice-sheet modelling. As on-site measurements in remote areas are sparse, satellite-based measurements have to be used to obtain area-wide surface velocities. *Synthetic Aperture Radar* (SAR) data from various sensors are routinely employed for this purpose. Depending on the availability of adequate SAR image pairs, the surface velocity can be derived by SAR interferometry. The accuracy of the applied interferometric method heavily depends on external input parameters (e.g. elevation model) and the processing history.

The present thesis focuses on the hinterland of the German overwintering station Neumayer III (Antarctica) and complements pre-site surveys for a future deep drill ice core site. The dependency of the interferometric approach on external elevation models is tested by comparing surface velocities based on Antarctic-wide elevation models (from satellite altimetry) with surface velocities based on local elevation models (from SAR interferometry). The accuracy of the generated surface velocity fields is evaluated by comparing the data with on-site GPS measurements.

A map of surface velocities in the hinterland of the German overwintering station Neumayer III and a precise estimate of the grounding zone location are presented as geophysical results. The derived surface velocities cover an area of $\sim 17.000 \text{ km}^2$ of floating and grounded ice and are based on 16 SAR scenes from the *European Remote-Sensing Satellites* (ERS) 1/2 acquired between 1994-1996. The derived surface velocities vary between $0 \text{ m/d} - 0.5 \text{ m/d}$ with a locally varying error between $0.002 \text{ m/d} - 0.08 \text{ m/d}$.

Zusammenfassung

Oberflächengeschwindigkeiten polarer Eismassen sind ein wichtiger Parameter für die Modellierung von Eisschilden und deren Massenbilanzierung. Die allgemeine Unzugänglichkeit des antarktischen Kontinents erschwert großflächige Messungen vor Ort, weshalb vermehrt Satelliten gestützte Methoden verwendet werden. Unter anderem werden Radar-Satellitensysteme mit *Synthetischer Apertur* (engl. *Synthetic Aperture Radar* oder SAR) verwendet. Wenn SAR Bilder mit hinreichender Qualität verfügbar sind, können Oberflächengeschwindigkeiten mittels Radarinterferometrie bestimmt werden. Die Genauigkeit der hier angewendeten Methode hängt stark von externen Parametern (z.B. digitalen Geländemodellen) und den einzelnen Prozessierungsschritten ab.

Der regionale Fokus dieser Diplomarbeit liegt südlich der deutschen Überwinterungsstation Neumayer III (Antarktis) und ergänzt die Vorerkundungen für eine neue Eiskern Tiefenbohrung. In der vorliegenden Arbeit werden Geschwindigkeitsfelder basierend auf unterschiedlichen Geländemodellen (Antarktis weite Geländemodelle, die auf Satelliten Altimetrie Messungen beruhen, sowie regionale Geländemodelle, die auf Radarinterferometrie basieren) generiert und verglichen. Um die Genauigkeit der abgeleiteten Fließgeschwindigkeiten abschätzen zu können, werden diese, soweit möglich, mit lokalen GPS Geschwindigkeitsmessungen verglichen.

Als geophysikalisches Ergebnis werden sowohl eine Karte von Oberflächengeschwindigkeiten des Untersuchungsgebiet als auch eine genaue Kartierung der Aufsetzzone präsentiert. Die Inland- und Schelfeis Geschwindigkeiten konnten für eine Fläche von ca. 17.000 km² berechnet werden. Hierfür wurden 16 SAR Szenen verwendet die zwischen 1994-1996 von ERS-1 und ERS-2 (*ERS* - engl. *European Remote-Sensing Satellite*) aufgenommen wurden. Die berechneten Oberflächengeschwindigkeiten reichen von 0 m/t – 0.5 m/t und weisen einen örtlichen Fehler zwischen 0.002 m/t – 0.08 m/t auf.

Contents

1. Introduction	1
1.1. Goals of this study	3
1.2. Region of interest	3
1.3. Basics of ice dynamics	5
2. Satellite Radar Imaging	9
2.1. Real Aperture Radar (RAR)	9
2.2. Synthetic Aperture Radar (SAR)	11
2.3. Interferometric SAR	13
3. Overview of basic datasets	19
3.1. European Remote Sensing Satellite - 1/2	19
3.2. Digital Elevation Models (DEMs)	21
3.3. Ground control and validation	23
3.4. Comparison of DEMs used	25
4. Processing chain: From four satellite scenes to a three-dimensional displacement field	31
4.1. Interferogram generation	33
4.2. Separation of motion and topography	35
4.3. Phase unwrapping	38
4.4. Adjustment of unwrapped phase using Ground Control Points	40
4.5. Derivation of three-dimensional ice-flow using ascending and descending passes	43
4.6. Horizontal flow of the floating shelf ice	44
5. Evaluation of the three-dimensional velocity fields	47
5.1. Mosaicking	47
5.2. Processing uncertainties	49
5.3. Dependency of DEM accuracy on three-dimensional surface velocities	54
5.4. Comparison of calculated three-dimensional velocity field with ground truth data	57
6. Geophysical results	61

Contents

6.1. Grounding zone location	61
6.2. Ice flow in the Neumayer III hinterland	63
7. Summary and outlook	65
A. Appendix	67
A.1. Automation of the processing chain	67
A.2. Velocity profiles	69
Acknowledgments	71

List of Figures

1.1. Region of interest	4
1.2. Depiction of the Antarctic ice system (modified after Bell (2009))	6
1.3. Illustration of the grounding zone (after Fricker and Padman (2006))	7
2.1. Relation between phase, amplitude and wavelength	11
2.2. The principle of a SAR system	12
2.3. Setup for interferometric imaging	14
2.4. Sensitivity of ERS to vertical and horizontal motion (after Meyer (2004))	17
3.1. ERS satellite tracks used for InSAR processing	20
3.2. Elevation differences along airborne laser altimeter profiles	27
3.3. Location of profiles	28
3.4. Laser altimetry profile	29
3.5. GPS profile	29
4.1. Work flow in the production of a three-dimensional velocity field	32
4.2. Interferogram before and after flat-earth removal	35
4.3. Interferogram. Fringes caused by topography, surface displacement and tidal movement	36
4.4. Interferogram before and after subtracting topography	38
4.5. Interferogram before and after phase unwrapping	39
4.6. Three-dimensional illustration of the relation between GPS-derived velocity and the velocity along the satellite's LOS	40
4.7. Unwrapped 'motion-only' interferogram	42
4.8. One-dimensional flow field of an ascending and a descending satellite path	43
4.9. Three-dimensional velocity field	44
5.1. Mosaic of differences in overlapping areas	48
5.2. Differences between two three-dimensional velocity fields in overlapping area	50
5.3. Differences between aspect angle and flow direction	52
5.4. Comparison between calculated flow and hill slope	54
5.5. Comparison between surface velocities based on different DEMs	55

List of Figures

5.6. Location of GCPs used for adjustment and evaluation of the calculated velocity field	57
5.7. Location of profiles in the region of the main ice flow	59
5.8. Profile 2 in the region of the main ice flow	59
6.1. Grounding line detection from different sources	62
6.2. Ice flow in the Neumayer III hinterland	64
A.1. Basic structure of the Python script <i>3D_DISP.py</i>	67
A.2. Profiles along and across an ice stream	69
A.3. Profile along an ice stream	70
A.4. Profile across an ice stream	70

List of Tables

- 1.1. Cryospheric components (modified after Lemke et al. (2007)) 1
- 3.1. ERS satellite tracks used for InSAR processing 21
- 3.2. GPS-derived flow vectors (modified after Riedel (2002)) 24
- 3.3. Available DEMs 25
- 5.1. Comparison of calculated flow velocities with GPS measurements 58
- 6.1. Three-dimensional velocity fields used for the final mosaic 63

List of Abbreviations

ALS	Airborne Laser Scanner
AMI	Active Microwave Instrument
ASAIID	Antarctic Surface Accumulation and Ice Discharge
ASTER	Advanced Spaceborne Thermal Emission and Reflection Radiometer
AWI	Alfred-Wegener-Institute for Polar and Marine Research
DEM	Digital Elevation Model
DEOS	Delft Institute for Earth-oriented Space Research
DML	Dronning Maud Land
ERS	European Remote-Sensing Satellite
ESA	European Space Agency
GCP	Ground Control Point
GLAS	Geoscience Laser Altimeter System
GPR	Ground Penetrating Radar
GPS	Global Positioning System
GRACE	Gravity Recovery and Climate Experiment
ICESat	Ice, Cloud and Land Elevation Satellite
InSAR	Interferometric SAR
IPCC	Intergovernmental Panel on Climate Change
LIMA	Landsat Image Mosaic of Antarctica

List of Abbreviations

LIMPICS	Linking micro-physical properties to macro features in ice sheets with geophysical techniques
LOS	Line Of Sight
METI	Ministry of Economy, Trade and Industry of Japan
MOA	MODIS Mosaic of Antarctica
MODIS	Moderate Resolution Imaging Spectroradiometer
NASA	National Aeronautics and Space Administration
NH	Northern Hemisphere
NSIDC	National Snow and Ice Data Center
RAMP	Radarsat Antarctic Mapping Project
RAR	Real Aperture Radar
RES	Radio Echo Sounding
RMSE	Root Mean Square Error
SLC	Single Look Complex
SLE	Sea Level Equivalent
SNR	Signal to Noise Ratio
SRTM	Space Shuttle Radar Topography Mission
TWT	Two Way Travel Time
USGS	U.S. Geological Survey

1. Introduction

The world's climate system consists of the compartments atmosphere, cryosphere, hydrosphere, lithosphere and biosphere (Dyck and Peschke 1995, p. 21). These compartments interact in a complex and sensitive way, causing the system's nonlinearity. Changes between the different compartments in this system, fostered by human interference, have unforeseeable effects for the world's climate. Among the most discussed developments is the rise of the global sea level, which is of great importance to both nature and society. In the last *Intergovernmental Panel on Climate Change* (IPCC) report, the average sea level rise for the 20th century is denoted with 1.7 ± 0.5 mm/a (Bindoff et al. 2007, p. 387). This development is attributed to increasing temperatures, causing a thermal expansion of water on the one hand and higher melting and evaporation rates on the other. As a result, there is an increasing inflow of fresh water into the oceans from the melting of the land ice masses of the polar regions and the higher mountains. The potential impact of the cryospheric components on the global sea level rise is listed in Table 1.1.

Table 1.1.: The area, volume and *sea level equivalent* (SLE) for the cryospheric components are given below. The annual minimum and maximum for snow, sea ice and seasonally frozen ground is shown, as well as the annual mean for the other components (partially only for the *Northern Hemisphere* (NH)). The sea ice area is represented by the region within the sea ice edge. Modified after Lemke et al. (2007, p. 342).

Cryospheric Component	Area (10^6 km ²)	Ice Volume (10^6 km ³)	Potential Sea Level Rise (SLE) (m) ¹
Snow on land (NH)	1.9–45.2	0.0005–0.005	0.001–0.01
Sea ice	19–27	0.019–0.025	0
Glaciers and ice caps ²	0.54	0.13	0.37
Ice shelves ³	1.5	0.7	0
Greenland ice sheet ⁴	1.7	2.9	7.3
Antarctic ice sheet ³	12.3	24.7	56.6
Seasonally frozen ground (NH) ⁵	5.9–48.1	0.006–0.065	0
Permafrost (NH) ⁶	22.8	0.011–0.037	0.03–0.10

¹ Assuming an oceanic area of 3.62×10^8 km², an ice density of 917 kg m⁻³, a seawater density of 1.028 kg m⁻³, and seawater replacing grounded ice below sea level.

² Dyurgerov and Meier (2005); glaciers and ice caps surrounding Greenland and Antarctica are excluded.

³ Lythe and Vaughan (2001).

⁴ Bamber et al. (2001).

⁵ Zhang et al. (2003).

⁶ Zhang et al. (1999), excluding permafrost under ocean, ice sheets and glaciers.

While it is evident that the melting of the ice sheet covering Antarctica would have the largest impact, it is also the most unlikely scenario. The melting of mountain glaciers and the Greenland ice sheet, however, is a more realistic threat (Rahmstorf and Schellnhuber 2007, p. 61). The Antarctic ice sheet stores more than 80% of the world's fresh water resources (Roland 2009, p. 241). As shown in Table 1.1, the unlikely collapse of the entire Antarctic ice sheet would result in a sea level rise of 56.6 m. However, also small changes in the overall Antarctic ice mass balance can strongly influence the global system.

In addition to changes in the sea level, melting of the Antarctic ice is expected to have serious consequences on the world's radiation budget. This is due to the loss of the high albedo of the Antarctic ice (Lemke et al. 2007, p. 341). Also, it is assumed that the thermohaline circulation would be disturbed by the melting of Antarctic ice and the resulting influx of freshwater into the ocean (Massom and Lubin 2006, p. 3). The mass balance of an ice sheet is quantified in terms of *accumulation*¹ versus *ablation*² (Massom and Lubin 2006, p. 11). An imbalance between inputs (e.g. snowfall) and loss (e.g. calving events, sublimation/evaporation, melt runoff) results in a change of mass balance. For mountain glaciers and the Greenland ice sheet melting and evaporation are the main ablation processes (Bentley and Thomas 2007, p. 102). In contrast, Antarctica loses ice mainly due to calving events at the coasts and along the shelf ice edge (Wilhelm 1975, p. 215). Whether the mass balance of the Antarctic ice sheet is positive or negative is not certain at the moment and is strongly dependent on the method applied. Chen et al. (2009, p. 859) estimate a total mass loss of 190 ± 77 Gt/a based on the *Gravity Recovery and Climate Experiment* (GRACE). Estimates from GRACE data are assumed to be the most accurate at the moment. The acquisition of the individual parameters influencing the mass balance of the large ice sheets remains a difficult task. This applies in particular for the acquisition of ground truth data (Eisen et al. 2008).

The *dynamic response time* of the polar ice sheets to climate change is much longer than for small mountain glaciers (Massom and Lubin 2006, p. 6). As a consequence, the response of the world's ice sheets to a global climate change remains the largest unknown parameter for the prediction of the future sea level rise (Massom and Lubin 2006, p. 10). Therefore, it is essential to monitor the mass balance of the Antarctic ice sheet more properly. Several programs pursue this target, including the European *ice2sea* (see, for example, Vaughan (2009)). A large potential for measurements on a wider scale is given by remote sensing techniques from airplanes and satellites.

Since the ice loss of the Antarctic ice sheet is a highly dynamic process, knowledge of the ice flow is essential for an understanding of the current state and for predicting future developments. As pointed out in Table 1.1, mass changes of ice shelves and

¹Accumulation: Positive mass budget, gained primary through snowfall.

²Ablation: Negative mass budget. Mass is lost by a number of mechanisms, which strongly depend on the local environment (e.g. supra and subglacial melting, wind erosion, iceberg calving etc.).

sea ice have no direct effect on the sea level, as they are not grounded. However, a removal of the ice shelves could speed up the displacement of grounded ice into the ocean, since they act like a stopper for the grounded ice sheet (Massom and Lubin 2006, p. 9). The potential force of this phenomena became apparent when the northern Larsen ice shelf on the Antarctic Peninsula collapsed in 1995 (Rott et al. 2002, 2010).

1.1. Goals of this study

The goals of this thesis are:

- to understand the difficulties associated with the interferometric processing used to derive surface velocities and to identify critical steps in this process.
- to automate the processing chain in order to find many SAR image pairs and to exchange processing parameters more easily.
- to analyze the dependency of the interferometric approach on external elevation models.
- to derive an area-wide velocity field with error estimates in the region of interest.
- to derive an estimate of the grounding zone location in the region of interest.

1.2. Region of interest

The region of interest (Figure 1.1) is situated in *Dronning Maud Land* (DML), Antarctica. Surface velocities could be derived for the region between 11° W - 6.6° W and 70.7° S - 72.8° S. Large parts of the survey area were first mapped during the Norwegian–British–Swedish Antarctic Expedition (1949-1952) (Riedel 2002, p. 63). The region around the Ekströmisen has a long tradition in German polar research as the overwintering stations Neumayer I-III were located there. The Ekströmisen is named after the Swedish engineer Bertil Ekström, who drowned after he dropped down the edge of the Quarisen in 1951. The new Neumayer III station, which was completed in February 2009, is located close to the Atka-Bay and is about 16 km south of the

1.2. Region of interest

shelf ice edge (Roland 2009, p. 47). The Ekströmsen is confined by the ice ridges Søråsen in the west and Halvfarryggen in the east.

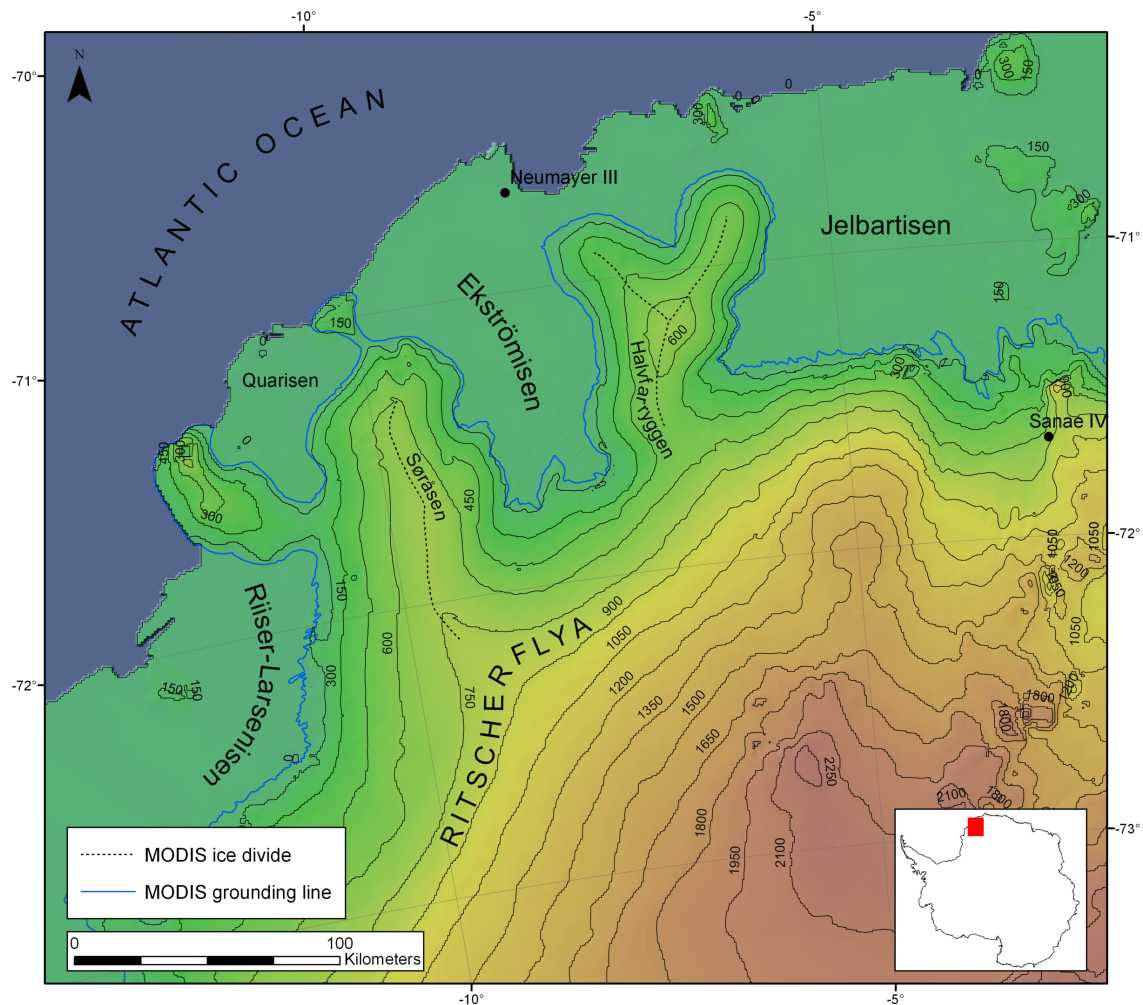


Figure 1.1.: Region of interest, hinterland of the German overwintering station Neumayer III. The South African overwintering station Sanae IV is located in the most eastern part of the map. Contour lines are located every 150 m and were derived from a combination of a local elevation model (Drews et al. 2009), an Antarctic-wide elevation model (Bamber et al. 2009) and Landsat photogrammetry data (unpublished data: NASA's Goddard Space Flight Center). The *Moderate Resolution Imaging Spectroradiometer* (MODIS) grounding line (estimate of the region which separates the grounded ice from the floating ice, see Chapter 1.2 for further explanations) is available to the public and can be downloaded at the *National Snow and Ice Data Center* (NSIDC) as well as the *MODIS Mosaic of Antarctica* (MOA) from which the ice divides were evaluated.

1.3. Basics of ice dynamics

An ice sheet (Figure 1.2) is defined as a mass of grounded ice which covers a whole continent or sub-continent with an ice thickness high enough to hide most of the underlying bedrock (Bentley and Thomas 2007, p. 100). Like most glaciers an ice sheet is fed by snow accumulation on its surface. As subsequent layers of snow build up, the accumulated snow becomes more compacted firn and is finally transformed into glacier ice. The ice is driven by gravity and flows downhill from the highest points of the interior towards the ocean (Bentley and Thomas 2007, p. 102). In general, three different mechanisms of glacial flow can be distinguished (Cuffey and Paterson 2010, p. 223): viscous-plastic deformation of ice, sliding of ice over the bed and deformation of the bed itself. Viscous-plastic deformation of ice is characterized by laminar flow. The vertical velocity profile of viscous-plastic ice deformation decreases with depth, but remains constant in the upper parts of the moving ice. Sliding of ice and deformation of the bed are often linked to each other when displacement occurs at the margin between the ice and a deformable bed (Cuffey and Paterson 2010, p. 223). If sliding of ice occurs on a rigid bed, there must be a thin layer of water on which the ice starts to slide. This thin layer of water occurs if the pressure on the bottom of the glacier is high enough to shift the melting point below the temperature of the surrounding ice (Meyer 2004, p. 32). Further, it can originate from geothermal heat flow or a combination of both factors. Deformation of the bed occurs when moving ice deforms a soft sedimentary bed, which limits the forces acting between bed and ice. Since both mechanisms occur at the bottom, the term *basal slip* can be used both for sliding of ice and deformation of the bed (Cuffey and Paterson 2010, p. 223). How these mechanisms of ice motion combine is highly dependent on the thermal properties of the ice and the properties of the underlying bed. Plastic deformation of ice produces relatively slow ice fluxes, whereas basal slip mechanisms enable faster flow velocities. The flow of an ice sheet is characterized as “*slow to moderate, varying gradually with distance...*” (Cuffey and Paterson 2010, p. 356), which suggests viscous-plastic deformation of ice in most places. The velocity of the nonchanneled, slow moving part of the ice sheet covering West Dronning Maud Land is given as 1-15 m/a (Hambrey and Alean 2004, p. 92). However, there are also ice streams, i.e. regions where the ice moves much faster than in the immediate vicinity. In a broader sense, ice streams include fast-flowing outlet glaciers (Cuffey and Paterson 2010, p. 360). Most ice streams flow along channels in the bedrock with crevassed shear zones separating them from the surrounding slow moving ice (Figure 1.2). The velocity of an ice stream increases towards the coast. Winsborrow et al. (2010, p. 57) suggest that it is not a single factor that governs the flow of an ice stream. In fact, topographic focusing, a soft sedimentary bed, subglacial meltwater and calving margins are believed to be the main influencing variables for fast ice flow. In Antarctica, the flowing ice sheet reaches the ocean at some point to form ice shelves

1.3. Basics of ice dynamics

along large parts of the coast. Ice shelves are fed by ice flow from the ice sheet, snow accumulation on the top and basal freezing of the underlying sea water. Ablation of ice shelves is caused by calving of icebergs and basal melting. If an ice shelf is grounded at some point, a dome-shaped ice rise may occur. Typical flow velocities of ice shelves range from a few hundred meters per year up to one kilometer per year at the front. Except for ice rises at a grounding point, there is no flow resistance at the bottom since the ice shelf is floating. Therefore, the ice shelf flow is governed only by a combination of longitudinal and side drags (Cuffey and Paterson 2010, p. 373).

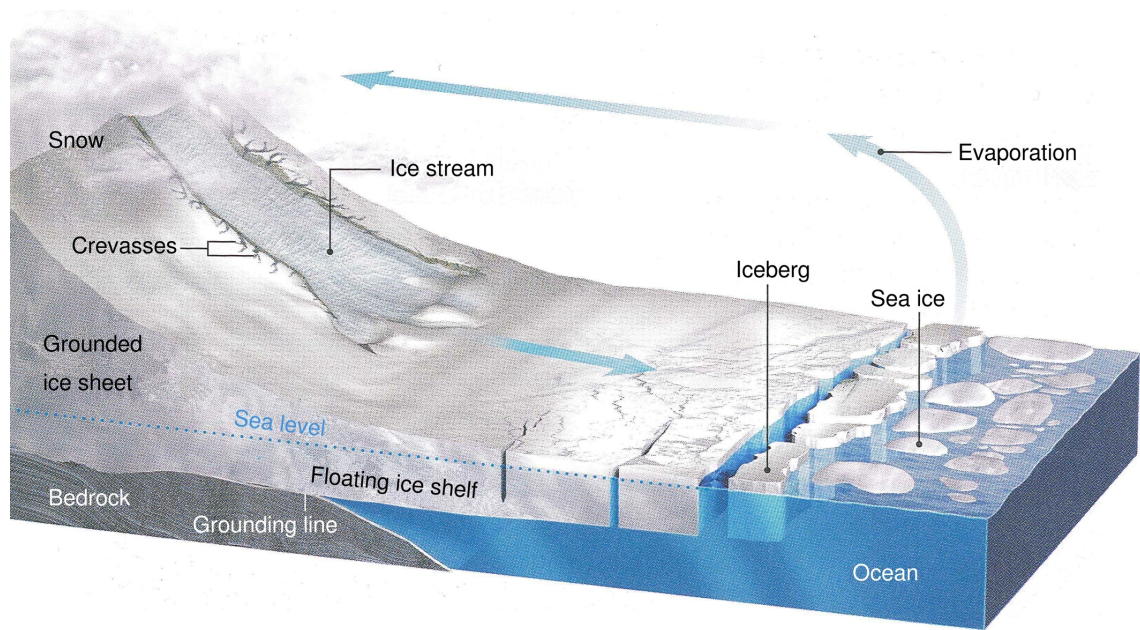


Figure 1.2.: Simplified depiction of the Antarctic ice system. Modified after Bell (2009, p. 36).

The transitional zone between the floating ice shelf and the grounded ice sheet is called *grounding zone*. Figure 1.3 shows a diagram of the grounding zone. The forces driving the motion of ice change drastically here, since the ice begins to float and basal melting occurs in the grounding zone.

The grounding zone can be defined as the area between F and H in Figure 1.3 and is typically a few kilometers wide (Sykes et al. 2009, p. 35). F indicates the position which limits the ice flexure from tidal movement and H indicates the point where the ice starts to float in hydrostatic equilibrium. The *grounding line* is the line along the bedrock where the ice starts to float, indicated as G in Figure 1.3, whereas I is the inflexion point where the ice is pressed below the hydrostatic level due to longitudinal stresses.

It is important to monitor the grounding line position, since its location may vary due to changes in ice thickness and sea level (Rabus and Lang 2002, p. 345). Also, ice

sheet/ocean modeling uses the grounding line as a boundary condition (Sykes et al. 2009, p. 35). Knowledge of the exact grounding zone position is needed for a correct interpretation of interferometric derived velocity data.

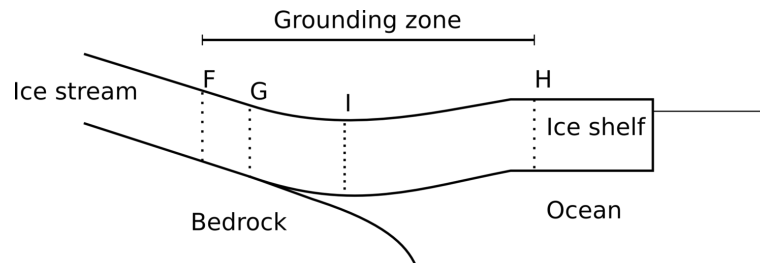


Figure 1.3.: Illustration of the grounding zone (after Fricker and Padman (2006, p. 2)).

2. Satellite Radar Imaging

Radar systems installed on airplanes or satellites are used for a wide range of applications in earth sciences. A radar system is used as an active remote sensing system which provides its own (microwave) illumination. This gives the radar system the ability to image in daylight or at night. The independence from external illumination is of great interest for the polar regions, since they are covered in darkness for a significant part of the year. Another advantage of a radar system is that microwaves can penetrate cloud cover. This results in the ability of the radar system to image in nearly all weather conditions. The independence from external illumination and the possibility to penetrate cloud cover are the main advantages of radar systems compared to optical imaging systems.

This section gives a general introduction to radar imaging systems. First, a short description about a radar system with a real aperture (RAR - *Real Aperture Radar*) is given. Secondly, the advantages of a *Synthetic Aperture Radar* (SAR) are discussed. This leads finally to SAR interferometry and its applicability in earth sciences. These principles are used later to derive surface velocities of ice in the hinterland of the German overwintering station Neumayer III.

2.1. Real Aperture Radar (RAR)

A radar system measures the *Two Way Travel Time* (TWT) of a microwave pulse. On airplanes or satellites, *nadir*¹-looking radars are used as altimeters which measure the distance between platform and ground via the conversion of the TWT to distance. After the time Δt the sensor of a radar system receives a part of the energy which was reflected from the ground. Δt is given by

$$\Delta t = \frac{2r}{c} \tag{2.1}$$

¹Nadir: Direction pointing directly below the sensor.

2.1. Real Aperture Radar (RAR)

where $2r$ is twice the distance between sensor and ground and c is the speed of light in the atmosphere. In a nadir looking mode, the system does not produce images because of the left-right ambiguity in runtime. In a side-looking geometry, images can be acquired as this ambiguity does not exist. A side looking radar uses a narrow microwave pulse which spreads perpendicular to the flight direction. The wavefront moves over the earth's surface in *range direction*² and the reflected signals are saved as rows in the radar image, relative to their travel time. After that, the radar system moves slightly along the *azimuth direction*³ and transmits the next microwave pulse. The reflection of this microwave pulse is recorded in the same way as before, but is represented in the next column of the radar image (Albertz 2007, p. 56 f.). Equation (2.2) shows that the resolution in range (Rr_{ra}) is strongly dependent on the pulse duration t_p of the transmitter

$$Rr_{ra} = \frac{c \cdot t_p}{2}. \quad (2.2)$$

The longer the pulse, the more targets are hit simultaneously and are thus indistinguishable. Thus, it is evident that the shorter the duration of the microwave pulse the better the achievable resolution in range. However, due to technical reasons a sufficiently long pulse duration is needed to achieve a reasonable *Signal to Noise Ratio* (SNR) of the backscattered signal.

The resolution in azimuth direction Rr_{az} is traditionally defined by the width of the illuminated *footprint*⁴. The width of the footprint Rr_{az} is highly dependent on the aperture angle α_r and increases with the distance between sensor and ground. The aperture angle α_r is a function of the wavelength λ and antenna length L_r (Meyer 2004, p. 13). The resolution in azimuth direction Rr_{az} can be approximated by

$$Rr_{az} = r \cdot \frac{\lambda}{L_r} = r \cdot \alpha_r. \quad (2.3)$$

Equation 2.3 quantifies the interrelationship of the resolution in azimuth direction, the distance between satellite and ground and the length of the antenna. If ERS would map with a real aperture and an antenna length of 10 m, it would have an azimuth resolution of about 4 km. This means that only objects separated by at least 4 km in azimuth direction would be resolved. Consequently, the satellite should have a long antenna to achieve an acceptable resolution, which is a difficult technical task. A real aperture radar can be used effectively on airplanes, which do not have that much ground distance when compared to satellites. A synthetic aperture is the solution for a satellite-based system, to get an acceptable resolution in azimuth direction.

²Range direction: Direction perpendicular to the flight direction.

³Azimuth direction: In flight direction.

⁴Footprint: Ground area which gets illuminated by the satellite's signal.

2.2. Synthetic Aperture Radar (SAR)

As outlined above, a satellite system with a real aperture would achieve a coarse resolution in azimuth direction and is therefore not used on platforms in space. Remote sensing satellites like ERS-1 or the space shuttle ‘Endeavour’ during the *Shuttle Radar Topography Mission* (SRTM) used a SAR.

A SAR system is a coherent radar system which records the amplitude and phase of the backscattered signal. Figure 2.1 describes the relation between phase, amplitude and wavelength. In order to increase the spatial resolution in azimuth direction, several post-processing steps generally referred to as SAR processing, or focusing, are necessary (Massonnet and Feigl 1998, p. 442). SAR processing is a complex procedure, extensively discussed in the literature (see, for example, Cumming and Wong (2005)) and only the basic theory will be discussed here.

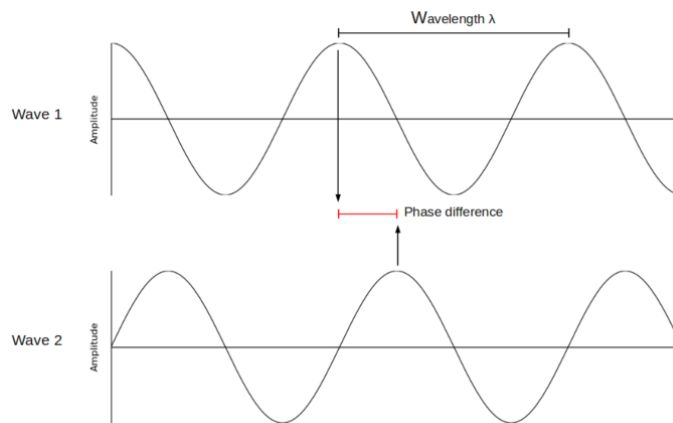


Figure 2.1.: Relation between phase, amplitude and wavelength. The amplitude of the backscattered signal complies with the brightness of the SAR image. The wavelength λ is fixed for a SAR.

To image in high-resolution along track a long radar antenna is simulated by a SAR. A relatively small antenna is used to transmit microwave pulses in a wide, club like manner. As the satellite moves between the transmission of two radar pulses, a point on the ground (see point P in Figure 2.2) gets illuminated several times during the pass of the satellite when the distance between the satellite positions of two successive pulse transmissions is much smaller than the length of the footprint (Rr_{az}). The SAR processing results in an image that can be imagined to be a coherent stack of the overlapping footprints. This means that the Doppler history of the individual targets within the scene is taken into account during the stacking procedure. The length of

2.2. Synthetic Aperture Radar (SAR)

a synthetic antenna can be described by the difference between the first and the last illumination of a ground target. If $S(t_1)$ in Figure 2.2 is the satellite position where P is illuminated the first time by the transmitted radar signal and $S(t_2)$ the position of the last time, the length of the synthetic aperture L_s can be defined by $S(t_2) - S(t_1)$.

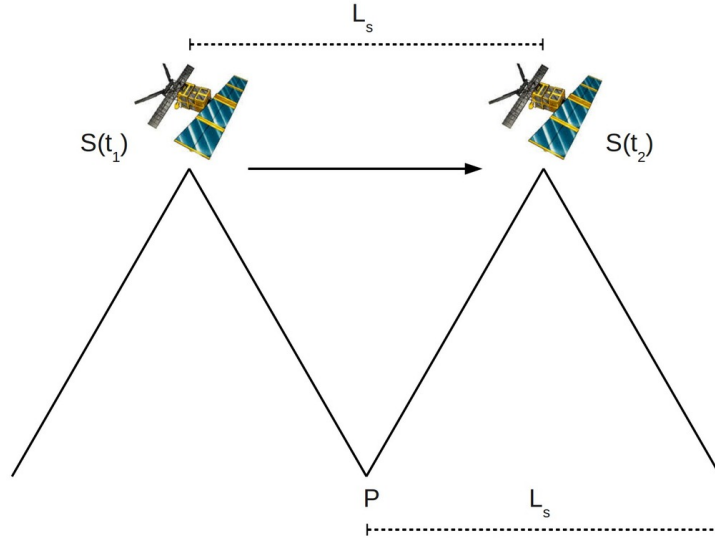


Figure 2.2.: The principle of a SAR system, with $S(t_1)$ and $S(t_2)$ as the satellite positions where P gets illuminated the first and the last time. L_s represents the length of the synthetic aperture.

For a SAR system, the resolution in azimuth direction can be described by (Meyer 2004, p. 14)

$$Rs_{az} = r \cdot \frac{\lambda}{2L_s}. \quad (2.4)$$

The width of the footprint (Rr_{az}) is given in equation (2.3). As a result (2.4) can be rewritten as

$$Rs_{az} = r \cdot \frac{\lambda}{2r \cdot \frac{\lambda}{L_r}} = \frac{L_r}{2}. \quad (2.5)$$

According to (2.5), the resolution in azimuth direction increases with decreasing an-

tenna size of the real aperture. This is at first counterintuitive, since for a RAR system a longer antenna leads to a better resolution in azimuth direction. However, in light of the coherent stacking procedure it makes sense since a larger footprint (e.g. a smaller antenna) covers the individual targets within the scene more often. In reality, relatively large antennas need to be installed on platforms in space to achieve sufficient energy in the backscattered signal (Meyer 2004, p. 14).

The coherent processing of the SAR data produces *Single Look Complex* (SLC) images. Such a SLC image can be regarded as a projection of the three-dimensional world into an x, y plane, where x is defined by the azimuth direction and y by the range direction. Every pixel in this image has a complex value and contains information of the phase and the amplitude of the backscattered signal.

A SAR image can be distorted by topographical effects. For example, *layover* effects may occur in mountainous areas: if two targets in a pulse line are within the same distance to the sensor, the resulting values in the SAR image are a mixture of both (Massonnet and Feigl 1998, p. 444). However, these effects can be neglected in the region of interest, since the area is relatively flat.

The phase which is saved in an SLC image appears as a value between 0° and 360° . For a single SLC image, the phase information is random due to the random scattering from the surface. The phase information of a single SAR image is therefore not of much use and can only be evaluated in a geophysical way when two SAR images are differentiated. SAR interferometry quantifies the difference between two complex SAR images, which is explained in the next section.

2.3. Interferometric SAR

The previous section discussed how large amounts of raw data can be processed to one high resolution SAR image, via the coherent post-processing of multiple (overlapping) footprints. These SLC images contain information of phase and amplitude for every pixel. The phase difference of two SLC images can be linked to topography and displacement. This is the main idea of the *Interferometric SAR* (InSAR) processing and will be discussed in more detail.

For InSAR to work, at least two SAR images of the same area acquired with a slightly different view angle need to be available. Figure 2.3 shows the geometrical setup for across-track SAR interferometry, whether for a *single-pass*⁵ or a *repeat-pass*⁶ system. The points i and j are the positions of the SAR during the image acquisition of the same area. The SAR positions i and j are separated through the spatial baseline B_{ij} . Differencing the phases of two SLC images acquired with a sensor constellation

⁵Single-pass system: Both SLC images are acquired at the same time by two SAR sensors.

⁶Repeat-pass system: The SLC images are acquired at different times.

2.3. Interferometric SAR

as shown in Figure 2.3 results in the interferometric phase $\Delta\phi_{ij}$. The interferometric phase $\Delta\phi_{ij}$ is dependent on the difference in *path length*⁷ $\Delta r = r_i - r_j$, and can therefore be approximated by

$$\Delta\phi_{ij} = \phi_j - \phi_i = \frac{4\pi}{\lambda} \Delta r \quad (2.6)$$

where ϕ_i and ϕ_j are the phase values of the SAR images acquired at the satellite positions i and j . Equation (2.6) can only be valid if the random scatter on the ground is equal for ϕ_i and ϕ_j . If this requirement is fulfilled, which is surprisingly often the case in Antarctica, the random scattering can be removed.

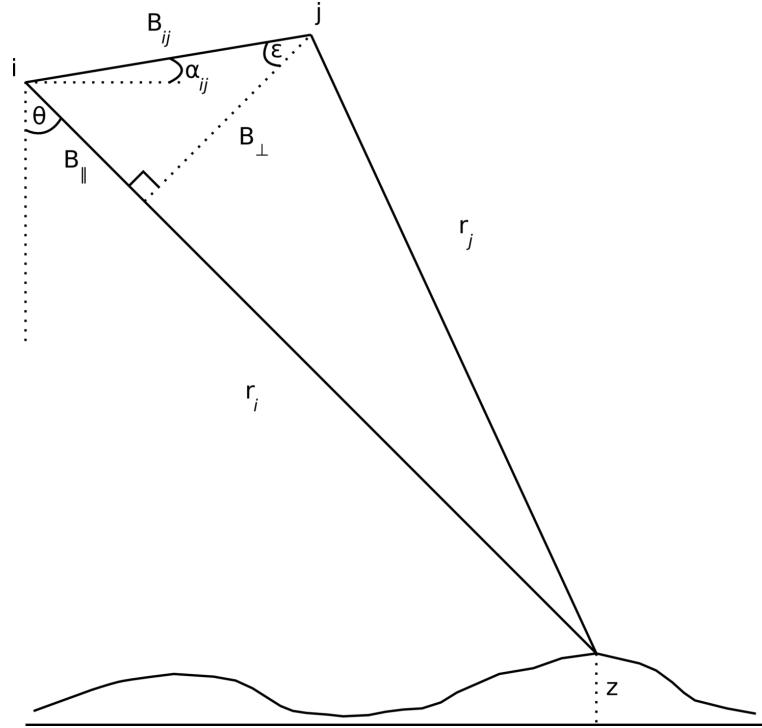


Figure 2.3.: Setup for interferometric imaging, the points i and j are the positions of the SAR during the data acquisition of the same area. θ is the look angle and B_{ij} the spatial baseline between the two SAR positions.

Equation (2.6) shows, that all contributions which affect Δr are reflected in $\Delta\phi_{ij}$. For a repeat-pass system, as used in this thesis, the single factors contributing to the interferometric phase $\Delta\phi_{ij}$ may be approximated by

$$\Delta\phi_{ij} = \Delta\phi_{orbit} + \Delta\phi_{topography} + \Delta\phi_{motion} + \Delta\phi_{atm} + \Delta\phi_{noise}. \quad (2.7)$$

⁷Path length: Distance between SAR and the surface.

To get information about surface motion ($\Delta\phi_{motion}$) and topography ($\Delta\phi_{topography}$) the other phase contents need ideally to be zero.

$\Delta\phi_{atm}$: is the phase difference due to atmospheric propagation delays. As the state of the atmosphere is not identical between image acquisitions, the interferometric phase is affected by an atmospheric propagation delay. The atmospheric propagation delay is discussed in more detail by Massonnet and Feigl (1998, p. 447).

$\Delta\phi_{noise}$: is the phase difference due to the two random scattering components on the snow covered surface. This component results most likely from unstable surface conditions between the dates of data acquisition (e.g. melting or accumulation of snow, rapid ice movement). A fundamental principle of InSAR to work is that the terms $\Delta\phi_{atm}$ and $\Delta\phi_{noise}$ need to be minimized. If the terms $\Delta\phi_{noise}$ and $\Delta\phi_{atm}$ are too large a proper InSAR processing cannot be guaranteed. Therefore, the *coherence* needs to be calculated to check the suitability of the specific SLC images for the InSAR processing.

The coherence γ is a statistical value which can be described as the degree of decorrelation between two complex SAR images and is expressed by (Rosen et al. 2000, p. 349)

$$\gamma = \frac{\langle g_1 g_2^* \rangle}{\sqrt{\langle |g_1|^2 \rangle \langle |g_2|^2 \rangle}} \quad (2.8)$$

where g_1 and g_2 is the backscattered signal received at the respective SAR antenna and $\langle \cdot \rangle$ denotes the expected value. In practise, the latter is approximated by spatial averaging. The coherence γ is defined for the range between $[0, 1]$, where $\gamma = 1$ represents the maximum degree of coherence and $\gamma = 0$ the minimum degree of coherence (Meyer 2004, p. 25). As a rule of thumb, a coherence value of 0.3 is noisy but still usable for SAR interferometry, whereas a value of 1 represents excellent coherence, but is very rare (Massom and Lubin 2006, p. 69).

$\Delta\phi_{orbit}$: describes the phase difference due to the different acquisition geometry of the SAR sensors. If the acquisition geometry is known, $\Delta\phi_{orbit}$ can be simulated and thus be removed from the interferogram with the help of a reference ellipsoid. If this has been done correctly $\Delta\phi_{orbit} = 0$ can be assumed.

After the removal of $\Delta\phi_{orbit}$ the interferometric phase $\Delta\phi_{ij}$ of a coherent interferogram can be approximated by

$$\Delta\phi_{ij} = \Delta\phi_{topography} + \Delta\phi_{motion} \quad (2.9)$$

where the phase difference induced by topography ($\Delta\phi_{topography}$) is dependent on the spatial baseline B_{ij} and the phase difference induced by motion ($\Delta\phi_{motion}$) is dependent on the temporal baseline ΔT .

In Figure 2.3 the spatial baseline B_{ij} is composed into B_{\parallel} and B_{\perp} by projecting position j on r_i . Since

$$\alpha_{ij} + (90^\circ - \theta) + 90^\circ + \varepsilon = 180^\circ, \varepsilon = \theta - \alpha_{ij} \quad (2.10)$$

B_{\parallel} can be defined by $B_{ij} \sin(\theta - \alpha_{ij})$ and B_{\perp} by $B_{ij} \cos(\theta - \alpha_{ij})$. According to Rosen et al. (2000, p. 345) (2.9) can be approximated by

$$\Delta\phi_{ij} = \frac{4\pi}{\lambda} B_{ij} \cos(\theta_0 - \alpha_{ij}) \frac{z}{\rho_0 \sin(\theta_0)} + \frac{4\pi}{\lambda} \Delta\rho \quad (2.11)$$

where θ_0 describes the look angle to a constant reference surface and ρ_0 indicates the radar range to the reference surface. The topographic height above the reference surface is given by z . Surface displacement between the dates of data acquisition is indicated by $\Delta\rho$ and will be discussed later.

The sensitivity of the specific SLC image pair to topography depends mainly on the magnitude of B_{\perp} and can be approximated by the *altitude of ambiguity*. The altitude of ambiguity quantifies the change in topography needed to induce a phase shift of 2π . The altitude of ambiguity is dependent on the perpendicular baseline B_{\perp} and is given by (Massom and Lubin 2006, p. 50)

$$z2\pi = \frac{\lambda r \sin(\theta)}{2 B_{\perp}} \quad (2.12)$$

where r is the range distance between sensor and target. It is evident from (2.12) that the sensitivity to topography increases with the magnitude of the perpendicular baseline B_{\perp} .

The motion-induced interferometric phase component $\Delta\phi_{motion}$ in (2.9) is related to the displacement of the earth's surface between the times of data acquisition. This component can only be measured by a repeat-pass system since a time difference between image acquisitions at position i and j (Figure 2.3) is required. If this is the case, motion of ice in the satellite's *Line Of Sight* (LOS) can be detected. A displacement in general is calculated by

$$\boldsymbol{\delta} = \boldsymbol{x}(t_j) - \boldsymbol{x}(t_i) \quad (2.13)$$

where, for example, an ice particle which is located on position \boldsymbol{x} at time (t_i) moves to a new position $\boldsymbol{x}(t_j)$ at some later time. To get the average velocity \boldsymbol{v} between $\boldsymbol{x}(t_i)$ and $\boldsymbol{x}(t_j)$, the displacement $\boldsymbol{\delta}$ is divided by the time period ΔT , which is calculated by $\Delta T = t_j - t_i$. If t_i and t_j in (2.13) are the times of image acquisition at the satellite's position i and j (Figure 2.3), the displacement which is detectable by the satellite can be described by (Kwok and Fahnestock 1996, p. 190)

$$\Delta\rho = \boldsymbol{v} \cdot \hat{\boldsymbol{r}} \Delta T. \quad (2.14)$$

Since the satellite detects only the displacement along its LOS, \boldsymbol{v} is projected onto the LOS by $\boldsymbol{v} \cdot \hat{\boldsymbol{r}}$ where $\hat{\boldsymbol{r}}$ is the unit vector pointing from the ground target towards the satellite. As a result, $\Delta\phi_{motion}$ in (2.7) is described by

$$\Delta\phi_{motion} = \frac{4\pi}{\lambda} \Delta\rho. \quad (2.15)$$

⁸Vectors are indicated in bold font throughout this thesis.

As the look angle θ is relatively steep for ERS ($\sim 23^\circ$ at the scene center), the sensitivity is greater for vertical displacement than for horizontal displacement (Figure 2.4). According to Figure 2.4 is the sensitivity to horizontal displacement given by $\Delta\rho = \sin(\theta) \cdot \Delta hor$ and to vertical displacement by $\Delta\rho = \cos(\theta) \cdot \Delta ver$.

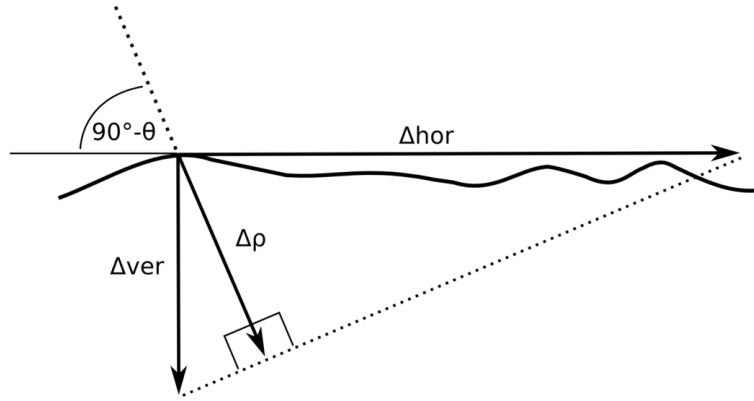


Figure 2.4.: Sensitivity of ERS to vertical (Δver) and horizontal (Δhor) motion (after Meyer (2004, p. 29)).

For a 2π phase shift, this leads to

$$H2\pi = \frac{\lambda}{2 \sin(\theta)} \quad (2.16)$$

for horizontal motion and to

$$V2\pi = \frac{\lambda}{2 \cos(\theta)} \quad (2.17)$$

for vertical motion. As a result, for ERS a motion-induced phase shift of 2π is related to horizontal displacement of 7.24 cm or vertical displacement of 3.07 cm at the scene center (Rack et al. 2000, p. 206). This shows the very high sensitivity of this method towards surface displacement.

If there were no spatial baseline B_{ij} , the phase difference would represent the ice displacement without any topographical component. Since passing the exact spot twice is technically impossible the phase information $\Delta\phi_{ij}$ of an interferogram which is constructed with a satellite constellation as shown in Figure 2.3 consists of a topographical part which is dependent on the spatial baseline B_{ij} and a part representing the displacement in the LOS direction (towards or away from the sensor) which is dependent on the temporal baseline ΔT . One has to keep in mind, that small baselines are more sensitive to motion mapping, whereas large baselines favour topography.

3. Overview of basic datasets

In this chapter, the datasets on which the derived flow fields are based are introduced. In the first place, the ERS data are presented, followed by external *Digital Elevation Models* (DEMs). DEMs are an important input parameter for the interferometric approach which is used to derive surface velocities. This can be understood by looking at (2.9), where a subtraction of $\Delta\phi_{topography}$ would lead theoretically to pure displacement along the satellite's LOS. In this study, $\Delta\phi_{topography}$ is simulated from different datasets. For this, available DEMs in the region of interest are analyzed and compared with laser altimetry data and *Global Positioning System* (GPS) measurements. Also, GPS-based flow velocities are introduced. These are used for the adjustment and evaluation of the final flow velocities.

3.1. European Remote Sensing Satellite - 1/2

ERS-1 and ERS-2 are two almost identical earth observation satellites run by the *European Space Agency* (ESA). ERS-1 was launched in July 1991, followed by ERS-2 in April 1995 (D'Elia and Jutz 1997, p. 1). The most important instrument onboard both satellites is the *Active Microwave Instrument* (AMI). The AMI is a C-band instrument which combines a SAR and a Wind Scatterometer. The SAR can operate in image and in wave mode. In image mode, a wide swath of about 100 km is recorded, while in wave mode smaller images of about 5 km x 5 km are produced. The wave mode is used to measure length and direction of ocean waves and is of no further concern here, as the data used were solely recorded in image mode. The SAR within the AMI is a side-looking aperture with a look angle of 23° (see θ in Figure 2.3) at the scene center and a wavelength λ of 5.66 cm. The ground range resolution of the SAR is 20 m across track and 5 m along track. The Wind Scatterometer is used to detect wind speed. Since the AMI is a joint instrument, it is not possible to acquire both types of data at the same time. Another disadvantage is that the SAR instrument requires considerable power and can therefore only be used for 12 minutes per orbit. The data can only be collected within the range of a suitable ground station since the amount of data is too large for on-board storage (Cracknell 2001, p. 87).

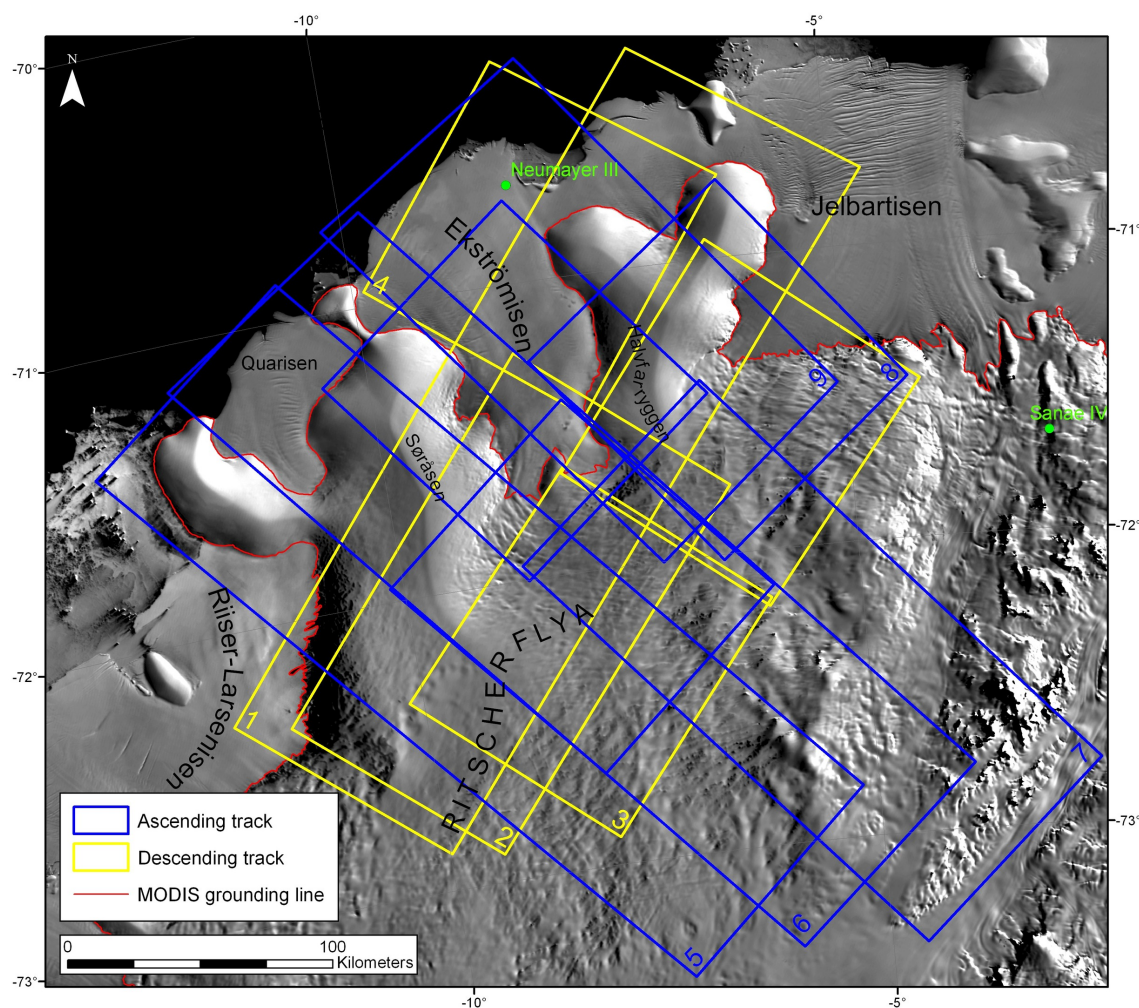


Figure 3.1.: ERS-1 & ERS-2 satellite tracks used for InSAR processing. Table 3.1 gives additional information about the shown satellite tracks. In the background is the NSIDC MODIS mosaic of Antarctica (MOA).

ERS-1 and ERS-2 were in a near-polar orbit at a height of ~ 780 km until ERS-1 was shut down in March 2000. The satellite data of interest were recorded during the second *Ice Phase*, lasting from January 1994 to April 1994, and the *ERS Tandem Mission* which started on 17. August 1995. The first and second *Ice Phases* were carried out by ERS-1 only with a repeat pass cycle of three days. Three days is a relatively good time period for interferometric processing, since the surface conditions do not change significantly and a good coherence between two repeat passes can still be expected. During the *ERS Tandem Mission*, ERS-1 and ERS-2 orbited the Earth with a time difference of only one day. In terms of good coherence, this time span is even better than the temporal baseline of the two *Ice Phases*, however it is less

sensitive to surface displacement. The ERS satellite tracks which were used for the interferometric derivation of ice flow are shown in Figure 3.1.

Table 3.1 gives additional information to Figure 3.1. The track and frame number used, the date of data acquisition and the direction of the satellite pass are listed here. The latter is important for the generation of a three-dimensional velocity field, as the satellite only detects motion in its LOS. The combination of an ascending satellite pass and a descending satellite pass gives the user information of two-dimensional ice flow (see Chapter 4.5). The ERS satellite data is available either as ESA processed SLC data or was processed from raw data for the generation of a local InSAR DEM (Drews et al. 2009).

Table 3.1.: ERS-1 & ERS-2 satellite tracks as shown in Figure 3.1. The official ESA track and frame number are listed below, as well as the date of data acquisition and the direction of the satellite pass.

ID	Track	Frame	Date	Pass
1	493	5121,5103,5085	18/19 Feb 1996	Descending
2	221	5121,5103	05/06 Mar 1996, 09/10 Apr 1996	Descending
3	178	5121,5103	06/07 Apr 1996	Descending
4	035	5085	12/13 Mar 1997	Descending
5	031	5661,5679,5697	06/09 Mar 1994 (2nd Ice Phase)	Ascending
6	045	5661,5679,5697	13/14 Mar 1997, 22/23 Feb 1996	Ascending
7	002	5661,5679,5697	15/16 Jan 1996	Ascending
8	188	5697	03/04 Mar 1996	Ascending
9	460	5697,5715	22/23 Mar 1996	Ascending

3.2. Digital Elevation Models (DEMs)

Accurate DEMs play an important role for the generation of three-dimensional flow fields. The *Space Shuttle Radar Topography Mission* (SRTM) which was carried out in February 2000 acquired elevation data with high spatial resolution. Unfortunately, there are no SRTM datasets for the polar regions as data acquisition took place between 60° latitude north and 56° latitude south only (Massom and Lubin 2006, p. 44). Therefore, other sources need to be employed to get elevation data for the polar regions. An overview of the available DEMs in the region of interest is given in the following.

ASTER GDEM: The Aster GDEM was released in 2009 in a cooperation between the *Ministry of Economy, Trade and Industry of Japan* (METI) and the *National Aeronautics and Space Administration* (NASA). The imaging instrument *Advanced Spaceborne Thermal Emission and Reflection Radiometer* (ASTER) uses 14 spectral bands for image acquisition, amongst others a near-infrared band. The near-infrared

3.2. Digital Elevation Models (DEMs)

band additionally is acquired using a backward-looking telescope. Therefore, along track topographical mapping is possible using a stereo-correlation method. The generated elevation data has a spatial gridding of 30 m x 30 m.

Bamber DEM: The ‘Antarctic 1 km Digital Elevation Model (DEM) from Combined ERS-1 Radar and ICESat Laser Satellite Altimetry’ (Bamber et al. 2009) (hereafter referred to as Bamber DEM) is a combination of laser altimetry measurements from ICESat’s *Geoscience Laser Altimeter System* (GLAS) and satellite radar altimetry data, acquired during the geodetic phase of ERS-1, which started in September, 1994 (D’Elia and Jutz 1997, p. 2). ICESat laser altimetry data has a very good vertical resolution but a poor spatial resolution, while the ERS-1 radar altimeter data has a good spatial coverage, but a poorer vertical resolution. For the Bamber DEM, a spatial gridding of 1 km x 1 km was chosen (Bamber et al. 2009, p. 101). The Bamber DEM is available to the public and can be downloaded at the *National Snow and Ice Data Center* (NSIDC). At the moment, it is considered to be the most accurate Antarctic-wide elevation model.

Landsat DEM: The Landsat DEM was derived by photoclinometry and has a spatial gridding of 15 m x 15 m. Photoclinometry is a technique which quantitatively relates the brightness of a visible or near-infrared pixel in a satellite image to surface reflectivity and local slope orientation with respect to the sun (Massom and Lubin 2006, p. 235). The photoclinometry data was derived from Landsat imagery and GLAS data was used to determine the photoclinometry scaling coefficient. The data is available within the *Antarctic Surface Accumulation and Ice Discharge* (ASAID) (Bindschadler 2007) project at NASA’s Goddard Space Flight Center. If the photoclinometrical approach works, accurate elevation data can be derived with this method. An example is shown in Figure 3.5. Photoclinometry data is available only for small coastal areas since a lack of contrast is observed in more continental areas. Areas of available photoclinometry data in the region of interest are colored green in Figure 3.3.

Local InSAR DEM: The local InSAR DEM was generated in 2009 at the *Alfred-Wegener-Institute for Polar and Marine Research* (AWI). It has a spatial gridding of 50 m x 50 m and covers most parts of the survey area, except for the floating shelf ice. It is based on an InSAR approach using SAR data from ESA’s ERS-1/2 including the SAR images shown in Figure 3.1. The interferometric derived elevation information was combined with laser altimeter data from ICESat’s GLAS (Drews et al. 2009).

RAMP DEM: The Antarctic-wide *Radarsat Antarctic Mapping Project* (RAMP) DEM is a combination of many different methods, amongst others: GPS, satellite ERS-1 radar altimetry and *Radio Echo Sounding* (RES). The spatial gridding is given as 200 m x 200 m, but parts of the model have a spatial gridding of 5 km x 5

km due to the different input datasets. The RAMP DEM is available to the public and can be downloaded at the NSIDC.

Wesche DEM: The local Wesche DEM was released by C. Wesche in 2009 (Wesche 2009). The region of interest is completely covered by this DEM. The spatial gridding is 2.5 km x 2.5 km. The DEM is interpolated through kriging and originates from different data sources, namely: kinematic GPS measurement, airborne radar altimetry, RES and GLAS laser altimetry.

3.3. Ground control and validation

The general inaccessibility of the Antarctic continent hampers the generation of high quality DEMs, which are by now standard for other parts of the world. For Antarctica, different remote sensing techniques are applied, each having its pros and cons, depending on the specific terrain. This is a challenge for every Antarctic-wide DEM which relies on one method only. Altimetry works great on the flat Antarctic plateau, but runs into problems in areas with higher surface slopes. Photoclinometry fails if the albedo changes due to varying snow conditions. Interferometry-derived DEMs are challenged by uncertain satellite trajectories and atmospheric conditions, and the list continues. Therefore, it is crucial to evaluate the DEMs with *Ground Control Points* (GCPs), if they are available. This section introduces the datasets which were used for an evaluation of the DEMs and for validation and adjustment of the final derived velocity fields. Airborne laser altimetry data is introduced first, followed by kinematic GPS measurements. Both datasets were used for the evaluation of the DEMs used. Kinematic GPS measurements were used for the validation and calibration of the calculated flow velocities.

Airborne laser altimetry data: The laser altimetry data of interest were recorded with an *Airborne Laser Scanner* (ALS) which was installed on the scientific aircraft *Polar 5* in 2007. The ALS was operated with 80 Hz and a scan angle of 45° (Helm et al. 2007, p. 2). The footprint of the ALS was about 1 m along track and 6 m across track. The deviation of the laser altimetry data to GPS measurement is within the range of centimeters. The ALS elevation data which is used in this study was interpolated to a 50 m x 50 m grid and serves as a precise reference base for the evaluation of the DEMs.

Kinematic GPS measurements: The kinematic GPS dataset shown as profile 2 in Figure 3.3 was recorded during a field campaign in January and February 2007. Local reference stations were used for the data processing (Wesche et al. 2009, p. 382). The

3.3. Ground control and validation

distance between the data points is given with 3 m. The vertical accuracy in elevation of the kinematic GPS data is in the order of centimeters to meters depending on the length of the baseline to the reference station.

As the region of interest is completely covered with ice, it is hard to find exposed bedrock where the surface displacement can be assumed to be zero. Such tie-points would be very valuable for the calibration and control of the satellite-derived flow velocities. Fortunately, sporadic GPS-derived velocity measurements are available in the region of interest (Riedel 2002, p. 66). The selected GPS velocity measurements are shown as arrows in Figure 3.3 and are listed in Table 3.2. The GCP *HALVFAR* in Table 3.2 was acquired in the same field campaign as the kinematic GPS measurement used for the DEM comparison (pers. comm. C. Wesche). The other GCPs listed in Table 3.2 were acquired during the *Polarstern* cruise *ANT XIV/3*. In this scientific cruise, an geophysical-geodetic field survey took place at the grounding zone of the Ekströmisen ice shelf (Riedel 2002, p. 66). One geodetic goal of the survey was to measure the response of the ice body to the ocean tides at different locations. Kinematic GPS measurements were carried out in the grounding zone in connection with a reference station on solid rock (Riedel et al. 1999, p. 240). Three-dimensional movement of the antenna positions could be derived from these measurements (Riedel 2002, p. 67). The velocity of the ice flow was measured as 27 m/a 30 km south of the grounding zone and varied between 75-148 m/a at the grounding zone. On the floating ice shelf, the flow accelerates up to 222 m/a at the shelf ice edge. The GPS points *GLSS* and *HALVFAR* (red arrows in Figure 3.3) were used for the calibration of the velocity of the grounded ice as the interferogram is most probably not affected by tidal movement in these areas (Chapter 4.2). GPS point *905* (Table 3.2) was used for the calibration of the velocity of the floating ice shelf.

Table 3.2.: GPS-derived flow vectors in the Ekströmisen ice shelf area. Modified after Riedel (2002, p. 66).

Station	Latitude [°]	Longitude [°]	Flow vector v [m/d]	α [°]	Time of measurement [d]
153	-70.698056	-9.222222	0.639726	325.3	11
305	-70.871111	-8.468889	0.506027	334.0	29
505	-71.044444	-8.477222	0.457534	337.4	13
705	-71.221667	-8.412778	0.458904	351.6	11
905	-71.401667	-8.347222	0.390137	358.5	10
1105	-71.578611	-8.325278	0.398630	22.3	13
1305	-71.720000	-8.521389	0.324384	23.6	12
GLN	-71.625278	-8.497222	0.405479	25.7	11
GLNM	-71.668611	-8.562500	0.396986	28.5	10
GL0	-71.709167	-8.622778	0.393699	31.4	10
GLSM	-71.752222	-8.664444	0.342466	27.0	10
GLS	-71.795556	-8.707222	0.205479	21.2	10
GLSS	-71.989444	-8.722222	0.075616	3.1	7
HALVFAR	-70.92568	-7.391785	0.01254	301.5	46

3.4. Comparison of DEMs used

In this section, the available DEMs in the region of interest are compared with airborne laser altimetry data. The DEMs which are finally used for simulating $\Delta\phi_{topography}$ are additionally compared with ground-based GPS measurements. Basic error estimation can be obtained by calculating the *Root Mean Square Error* (RMSE). To calculate the RMSE, a reference dataset needs to be available. In this study, the airborne laser altimetry dataset serves as a reference. For comparison, all datasets were resampled on a 125 m x 125 m grid. 11705 points derived from the laser altimetry dataset were used to calculate the RMSE for the available DEMs (Table 3.3). This value represents n in equation (3.1).

$$RMSE = \sqrt{\frac{\sum_{n=1}^n (i_1 - i_2)^2}{n}}. \quad (3.1)$$

In (3.1), i_1 is the same point from the DEM as i_2 from the laser altimetry dataset. Table 3.3 shows the RMSE for the available DEMs, except for the Landsat photogrammetry data, since the ALS data does not cover the Landsat DEM sufficiently.

Table 3.3.: Available DEMs for the region of interest. The spatial gridding is shown together with the RMSE based on airborne laser altimetry data. Also the coverage, method and source of the DEMs are listed.

Name	GRID	RMSE	Coverage	Method	Source
ASTER GDEM	30 m	894.9 m	World-wide	Stereo-correlation	NASA
Bamber DEM	1 km	40.5 m	Antarctic-wide	Laser-, radar altimet.	NSIDC
Landsat DEM	20 m	-	Coastal areas	Photogrammetry	NASA (unpubl.)
local InSAR DEM	50 m	12.3 m	Local	SAR interferometry	AWI
RAMP DEM	200 m	177.3 m	Antarctic-wide	GPS, radar altimet., RES	NSIDC
Wesche DEM	2.5 km	24 m	DML	GPS, laser-, radar altimet., RES	AWI

The RMSE shown in Table 3.3 varies strongly for the available DEMs. This shows the importance of testing the DEMs beforehand, if possible. For example, the RMSE of the global ASTER DEM is given as 21.19 m in the *ASTER Global DEM Validation Summary Report* (ASTER GDEM Validation Team 2009, p. 7). However, the RMSE in the survey area is about 42 times higher, perhaps due to the bad texture of the snow-covered surface in the survey area.

The calculated flow velocities in this study are based on the Bamber DEM and the local InSAR DEM. This is because of the high quality of both DEMs on the one hand and because of time constraints on the other. Nevertheless, the script which was written to automate the processing of flow velocity fields is designed for an easy

3.4. Comparison of DEMs used

input of different elevation datasets. For example, there are high expectations on the *TanDEM-X*¹ mission which was started in June 2010 (DLR 2010).

In the following, both elevation models used are compared again with ALS data and additionally with GPS field measurements to point out the spatial inaccuracy/accuracy of both elevation models in the survey area. The influence of the external elevation data on the final flow velocities is shown in Chapter 5.

Figure 3.2 illustrates the differences of the two DEMs with the available laser altimetry data. Obviously the local InSAR DEM leads to better results in this region, which can already be seen by looking at the margins of the color bars (Figure 3.2, top).

Furthermore, two profiles were taken for comparison in two relevant regions (Figure 3.3). Profile 1 is roughly perpendicular to the main ice flow into the Ekströmisen. Profile 2 is in the summit region of the ice ridge Halvfarryggen, a potential drill site for a deep ice core.

In profile 1, data from the laser altimetry dataset serves as a reference base and profile 2 is based on the kinematic GPS measurements. Figure 3.4 shows a profile of both DEMs along the laser altimetry profile 2 (top) as well as the differences to the laser altimetry data (bottom). The largest deviation of the local InSAR DEM is -20 m at one point (Figure 3.4, bottom), which again emphasizes the high accuracy of the InSAR DEM. Profile 2 (Figure 3.5) shows the photogrammetry data which was derived from Landsat imagery in comparison to the local InSAR DEM and the Bamber DEM. The photogrammetry data looks promising and appears to be very accurate in places, but is only available for small coastal areas since a lack of contrast is observed in more continental areas and is therefore of no further concern here. Nevertheless, a combination with elevation data from other sources could lead to interesting results (e.g. contour lines in Figure 1.1). The two other DEMs, the local InSAR DEM and the Bamber DEM, come off more badly in this area. This might be due to high accumulation rates in this region in the case of InSAR. High accumulation rates can lead to bad coherence as the surface conditions change significantly between the dates of data acquisition. For altimetry, this might be due to the relatively high surface slope. In conclusion, the local InSAR DEM compares better to GCPs than the Bamber DEM, which is nevertheless a very accurate elevation model on a larger scale.

¹TanDEM-X: Bistatic SAR mission, with two almost identical satellites flying in a close across-track formation for topographical mapping.

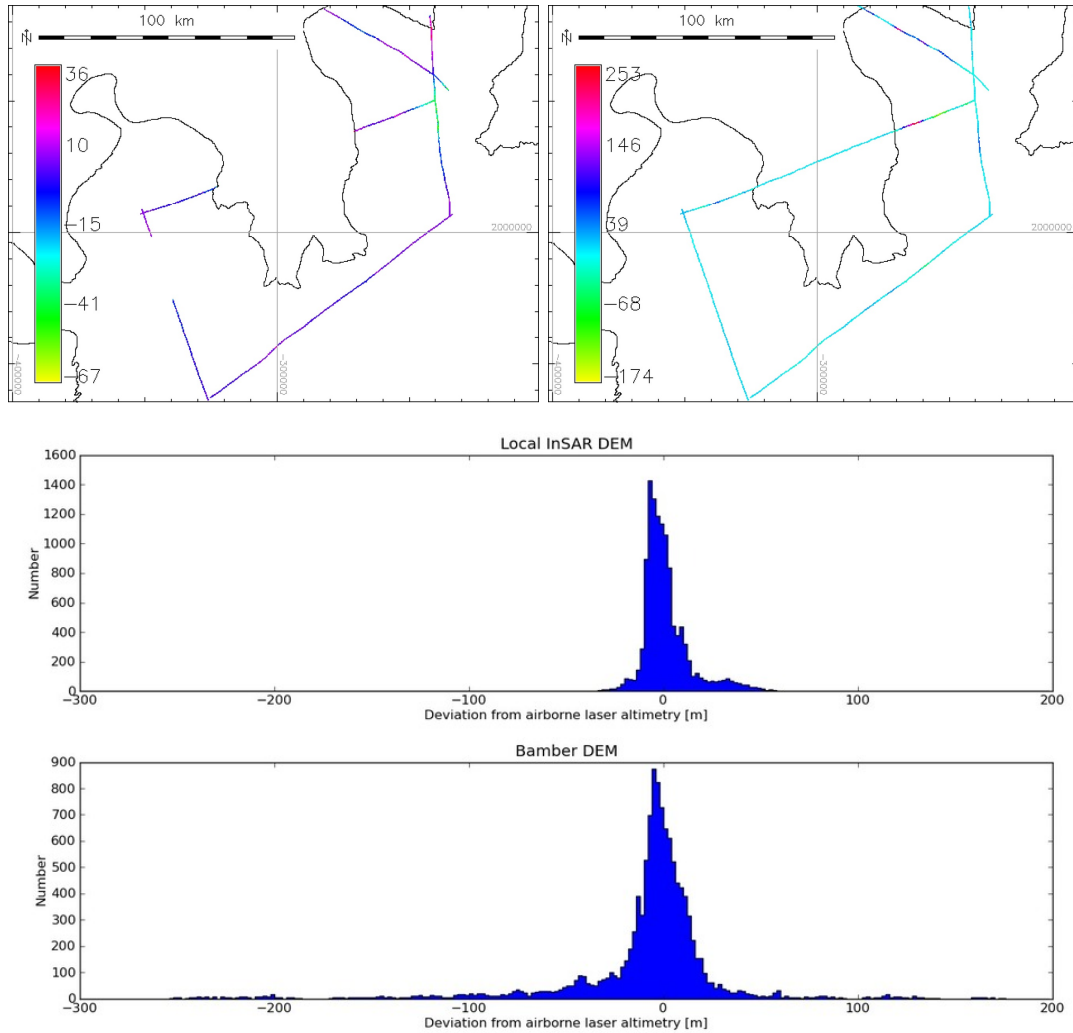


Figure 3.2.: Difference in meters along airborne laser altimetry profiles. Top left: local InSAR DEM (Drews et al. 2009), MODIS grounding line in the background. Top right: Antarctic-wide elevation model (Bamber et al. 2009), MODIS grounding line in the background. The deviation is much higher with the Antarctic-wide elevation model on the right-hand side. Bottom: Histograms of the deviation to the laser altimetry data.

3.4. Comparison of DEMs used

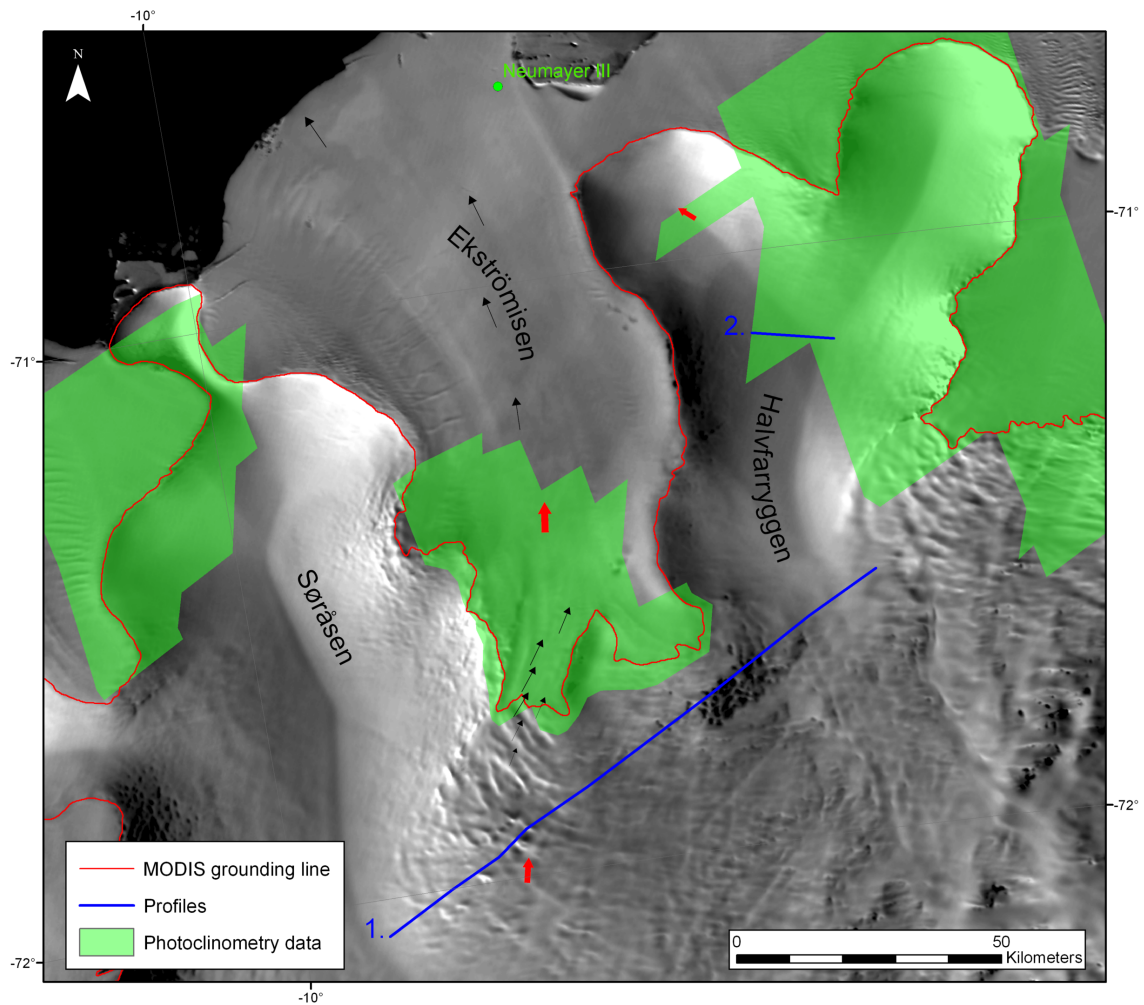


Figure 3.3.: Location of profiles for DEM comparison. 1 shows the laser altimetry profile (Figure 3.4) and 2 the GPS-derived profile (Figure 3.5). The arrows represent GPS-derived velocity measurements, and the red arrows indicate the GCPs which were used for velocity adjustment (Chapter 4.4). The green areas denote the availability of photoclinoetry data in this region. In the background is the NSIDC MODIS mosaic of Antarctica (MOA).

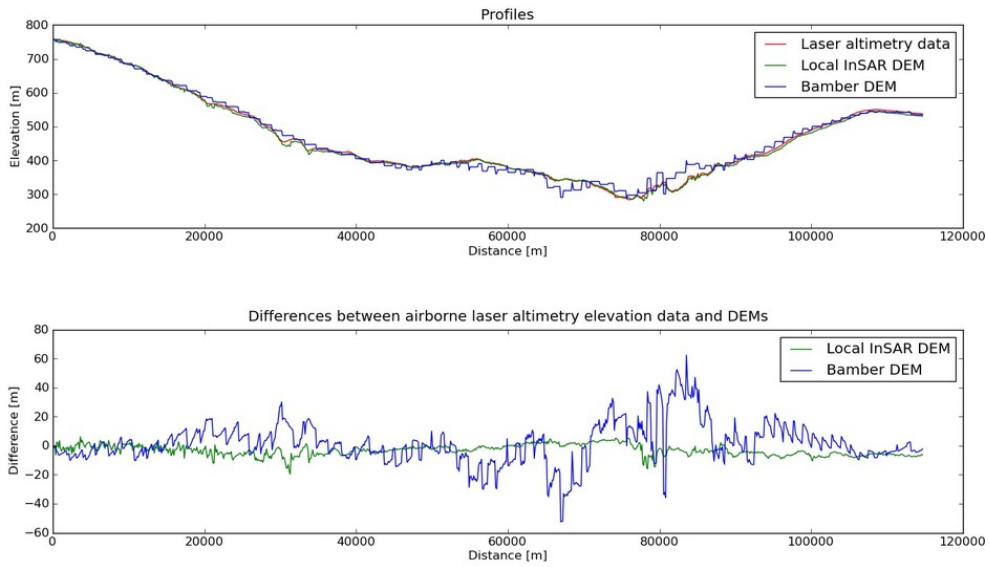


Figure 3.4.: Laser altimetry profile from profile 1 in Figure 3.3. Top: Profile along the Bamber DEM, the InSAR DEM and the airborne laser altimetry data. Bottom: Differences between the InSAR DEM and the Bamber DEM to laser altimetry data along the profile.

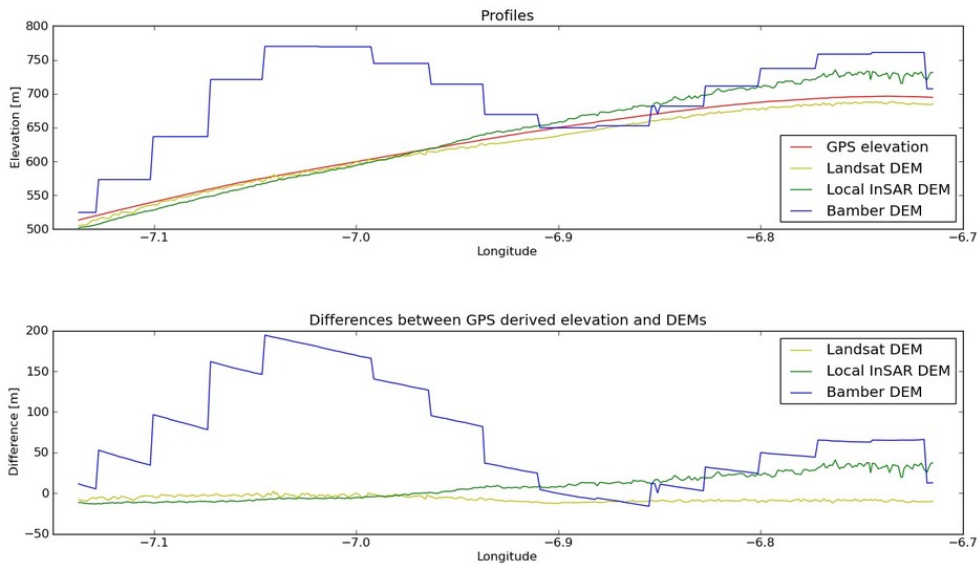


Figure 3.5.: GPS-measured profile from profile 2 in Figure 3.3. Top: Profile along the Bamber DEM, the InSAR DEM, the Landsat DEM and the kinematic GPS measurement. Bottom: Differences between the InSAR DEM, the Bamber DEM and the Landsat DEM to kinematic GPS measurement along the profile.

4. Processing chain: From four satellite scenes to a three-dimensional displacement field

Several three-dimensional velocity fields were generated with the aid of the commercial *GAMMA SAR and Interferometric Processing Software* from the datasets introduced in the previous Chapter. The *GAMMA* software is grouped into four modular software packages which process SAR data from various sensors. The modular software packages are:

- *Modular SAR Processor* (MSP)
- *Interferometric SAR Processor* (ISP)
- *Differential Interferometry and Geocoding Software* (DIFF&GEO)
- *Land Application Tools* (LAT)

The MSP is a module used for the processing of SAR raw data to SLC images (Werner et al. 2000)(Chapter 2.2). Several of the frames shown in Figure 3.1 were processed with this module for the generation of the local InSAR DEM (Drews et al. 2009) (as briefly described in Chapter 3.2). The remaining frames used in this work were processed by the German processing and archiving facility (D-PAF; Pfaffenhofen). The ISP module supports all necessary steps for the generation of interferometric products starting from SLC images. Several tools of the ISP were used for the data processing.

The DIFF&GEO module provides tools for differential interferometric processing as well as for geocoding satellite imagery. Geocoding and differential interferometry are included in the DIFF&GEO module since a coordinate transformation is required for the simulation of a ‘topography-only’ interferogram from external height data

(Werner et al. 2000). Many of these tools from the DIFF&GEO module were used in this study.

The LAT provides tools for simple classification schemes, multi-temporal analysis, statistics and image mosaicking (Wegmüller and Werner 2002), but is of no further concern here. Furthermore, there are several additional tools to display the processed data and interim results. The *GAMMA SAR and Interferometric Processing Software* runs on a UNIX system and is controlled via the command line and shell scripting.

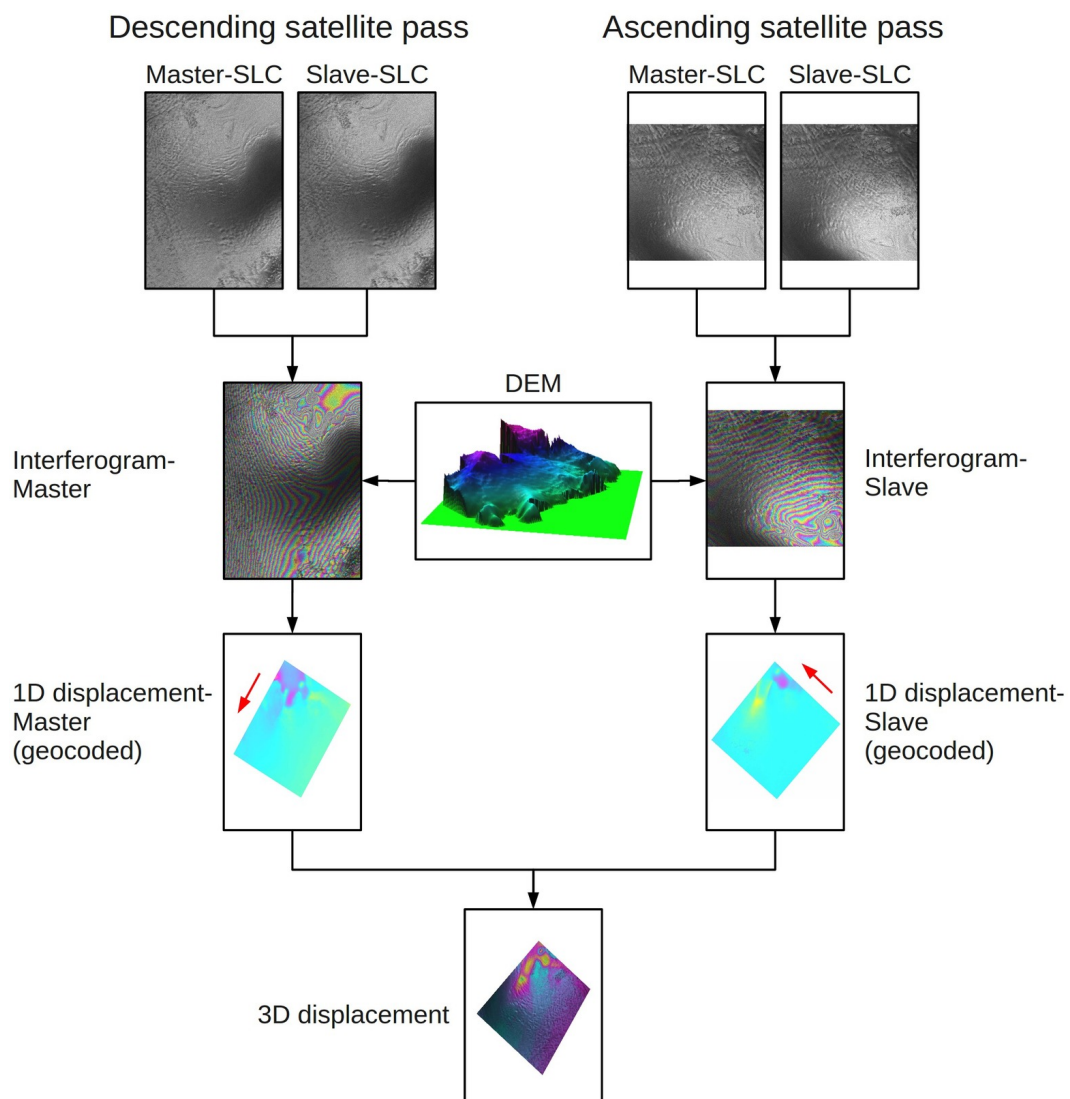


Figure 4.1.: Work flow in the production of a three-dimensional velocity field. The red arrows indicate the flight direction of the satellite.

This Chapter describes the individual processing steps employed to generate a three-dimensional velocity field. Figure 4.1 gives a broad overview of the complicated work flow. As shown in Figure 4.1, the first step towards a three-dimensional velocity field is the generation of two interferograms, one from a descending satellite pass and one from an ascending satellite pass. An interferogram is created by differencing two complex SAR images containing information about the phase and the amplitude of the backscattered signal. This interferogram holds information about the topography (depending on the spatial baseline) and the surface velocity (depending on the temporal baseline) (Chapter 2.3). Once two interferograms are created they need to be isolated from topography by subtracting a simulated ‘topography-only’ interferogram from external height data. Here the DEMs which are introduced in Chapter 3.2 come into play. As a one-dimensional velocity field represents only the velocity along the satellite’s LOS, the descending and ascending one-dimensional velocity fields are combined to form a three-dimensional velocity field after unwrapping the pure velocity interferograms. It turns out that the velocity fields calculated need to be corrected. In order to do this, the unwrapped phase was set to the X or Y component of a GCP point. The single steps of the flow field generation are described in more detail in the following sections.

4.1. Interferogram generation

The interferometric processing chain begins either with high-resolution SLC images, or with the unprocessed raw data, which must be converted into SLC images via a SAR processing step (Chapter 2.3). Two SLC images, recorded at slightly different spatial and temporal satellite positions (Figure 2.3) are combined to form one interferogram (Figure 4.1). The two SLC images should be based on the same SAR processor¹ for a proper interferometric processing. In this thesis, the interferometric processing starts either with already processed raw data (Drews et al. 2009) or ESA produced SLC imagery. An advantage of self processed SLC imagery is the ability to generate SLC segments larger than ESA-processed SLC segments. Discontinuities created by changing parameters may arise when combining ESA-processed SLC segments into one larger SLC segment (Massonnet and Feigl 1998, p. 455).

Starting with two SLC images, the first step towards an interferogram is the co-registration between the slave and the master SLC image. Which image is referred to as master and which as slave is chosen by the date of data acquisition as the younger image serves as the master SLC image. Co-registration means that each ground tar-

¹For example GAMMAs MSP module does not use a zero Doppler geometry, but the SLC images processed by the ESA do.

get must be localized to the very same position in both images. The master image serves as a reference on which the slave image is re-sampled, so the final interferogram has the same dimension as the master image. For the ERS satellites, a fixed shift in azimuth and range is typical. The shift in azimuth direction is mainly related to a different timing along track (Ferretti et al. 2007, p. 15), while the shift in range direction is due to a slightly different look angle between repeat passes (Kwok and Fahnestock 1996, p. 191). In a first approximation, the offset between the two images can be detected by visual comparison of the two intensity images and therefore unique features must be identifiable in both images. Another way to estimate a first offset would be to proceed from orbital parameters. Both approaches lead to a pixel-fine registration, but for interferogram creation a sub-pixel accuracy of better than 0.2 pixel is recommended (Wegmüller and Werner 2002). In order to achieve this goal, the image is divided in equal parts, where a cross-correlation for each fragment is implemented. This approach tries to match image parts with the same intensity. In the end, all image fragments are shifted by a calculated value and a two dimensional polynomial fit is performed. This step can be performed iteratively to get a more accurate result.

The actual differencing takes place once the two complex SLC images, each holding information about the phase and the amplitude of the backscattered signal, are matched properly. A complex conjugation of the co-registered slave image is performed, which changes the sign of its imaginary part. If a pixel in the conjugated image is defined as S^* , the phase difference between the master and the slave image can be calculated by MS^* , where M is the correspondent to S^* in the nonconjugated master image (Massonnet and Feigl 1998, p. 455).

A complex, multi-looking step with 2-looks in range and 10-looks in azimuth is executed during the interferogram computation. Multi-looking is an averaging procedure to minimize the phase noise in range and in azimuth directions. In order to reshape every pixel of the interferogram into an almost square-like format, it is recommended to average with a factor of 5 higher in azimuth direction than in range direction. This is because the resolution in azimuth direction is about 5 times higher than the resolution in range direction (Chapter 3.1).

As a result, an image of the phase difference at every co-registered pixel location is finally generated. Since the amplitudes of the two SLC images are averaged for every pixel, the interferogram contains information of the intensity at each pixel location as well (Massom and Lubin 2006, p. 54). For a graphical depiction, the phase difference is usually color coded with the intensity as grey-scale in the background. The color-coded phase information is represented by fringes. Fringes are lines with the same phase value and are usually pictured as a full color cycle (Figure 4.2). In an interferogram, one fringe represents a 2π phase shift. The newly created interferogram holds a mixture of orbital, topographical and surface displacement information (Chapter 2.3) but is dominated by orbital fringes (dense fringe pattern in Figure 4.2, left-hand side). Orbital fringes occur even in flat areas, because of different satellite distances

4. Processing chain: From four satellite scenes to a three-dimensional displacement field

during data acquisition and have to be removed with the use of a reference ellipsoid in a process called *flat-earth removal*. Therefore, the spatial baseline needs to be known since the phase trend expected for a smoothly curved earth is directly related to the sensor positions. The estimation of the spatial baseline is based on orbital information written in the *SLC parameter files*². If available, precise orbital information provided by the *Delft Institute for Earth-oriented Space Research* (DEOS) is used. The fringe pattern of the interferogram on the right-hand side of Figure 4.2 is solely related to motion and topography, as the flat-earth trend has already been removed.

The GAMMA tools which were used for the interferogram generation are within GAMMA's ISP module (see Wegmüller and Werner (2002) for further explanations).

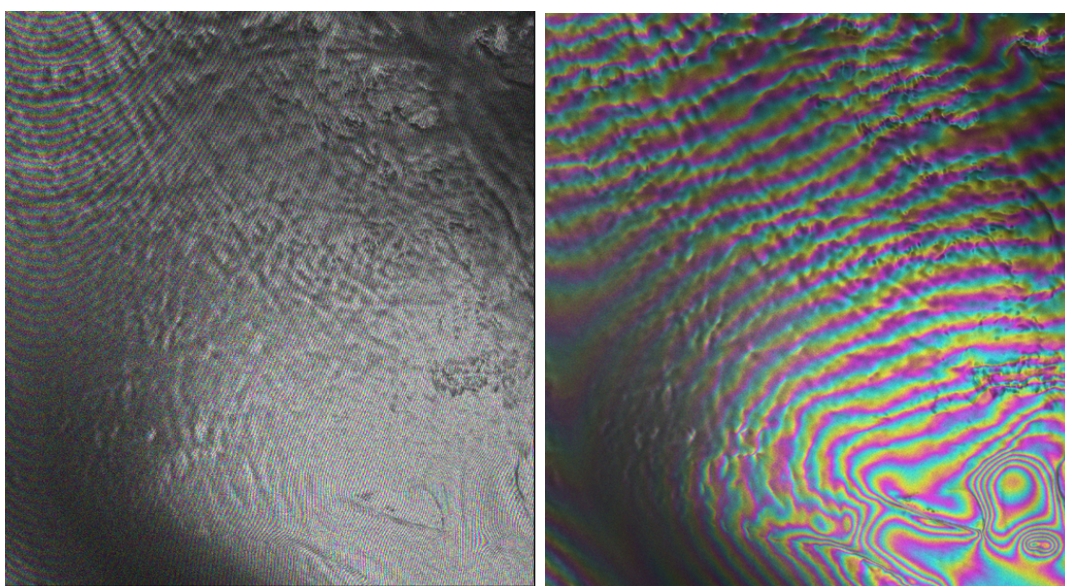


Figure 4.2.: Interferogram before and after flat-earth removal. The interferogram on the left-hand side is dominated by orbital fringes. The fringe pattern on the right-hand side is related to topography and motion only.

4.2. Separation of motion and topography

As mentioned above, the fringe pattern of a flattened interferogram is induced by surface displacement in the satellite's LOS and surface topography. The generated

²SLC parameter file: Contains information on the SAR sensor, the SAR processing, and the orbit geometry.

4.2. Separation of motion and topography

interferogram (Figure 4.3) shows mostly topographical effects, which are overlaid in some regions with ice flow. The fringes in a.) in Figure 4.3 are clearly related to topography, and can therefore almost be interpreted as contour lines. As explained in Chapter 2.3 the altitude of ambiguity describes the change in topography needed to induce a phase shift of 2π . The altitude of ambiguity can be regarded as the interval between the ‘contour lines’. Using GAMMA’s *base_perp* tool (within the ISP module), a perpendicular baseline of 158 m is calculated for the example interferogram at an incident angle θ of $\sim 23^\circ$. According to (2.12), this leads to an altitude of ambiguity of about 61 m for the topographical fringes in Figure 4.3.

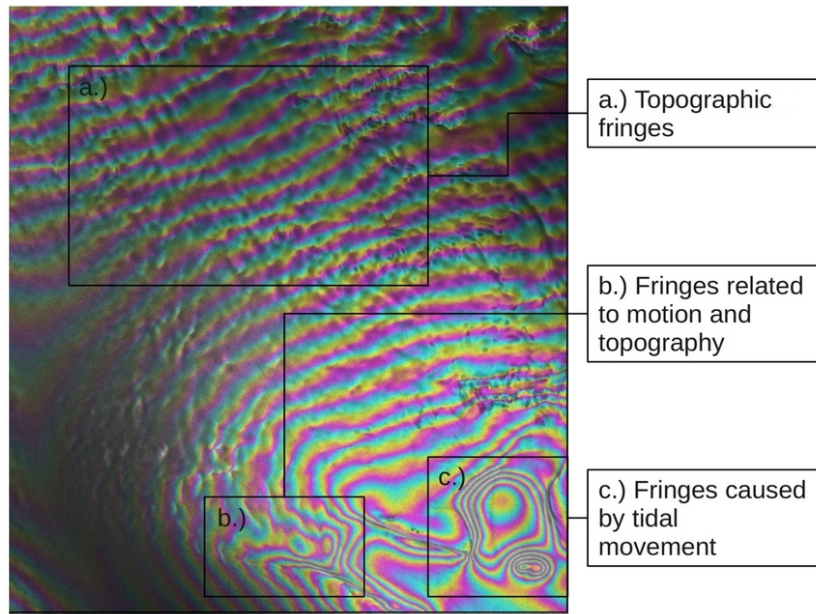


Figure 4.3.: Interferogram. Fringes caused by topography, surface displacement and tidal movement.

The fringes in b.) in Figure 4.3 are not as clearly delineated as in a.). Such a blurring of fringes suggests that these fringes are not related to topography only but are disturbed by horizontal surface displacement between the dates of data acquisition. An ambiguity of velocity can be calculated without any knowledge of B_{\perp} as the displacement-induced phase difference is completely independent of the spatial baseline. As noted in Chapter 2.3 for ERS a motion-induced phase shift of 2π is related to a vertical displacement of 3.07 cm or a horizontal displacement of 7.24 cm at the scene center (Rack et al. 2000, p. 206). This shows the very high sensitivity towards surface displacement compared to topographical effects.

The dense fringe pattern in c.) in Figure 4.3 is related to tidal (vertical) movement. If the tides are different between the dates of data acquisition this movement is reflected in a fringe pattern as shown in c.). Therefore the grounding zone, which represents

4. Processing chain: From four satellite scenes to a three-dimensional displacement field

the border between the grounded ice sheet and the floating shelf ice (Chapter 1.3), can be located relatively accurately from interferometric data (Chapter 6). The small closed formation of dense fringes in the lower part of c.) most probably indicates an ice rise (Chapter 1.3).

As already mentioned, the fringes in b.) (Figure 4.3) are related to relatively rapid motion, but are still mixed with topographical information. It is probable that the area shown as b.) in Figure 4.3 marks the flow of an outlet glacier. Such areas need to be isolated from topographical effects. The separation of motion and topography is explained in the following.

In order to eliminate the influences of topography in the interferometric phase, external elevation data is used. Therefore, a ‘topography-only’ interferogram is simulated from the external height data which was presented in Chapter 3.2. Before the actual simulation of the topographical phase, the relevant part of the DEM needs to be transformed from map coordinates into the geometry of the interferogram. This is achieved by resampling the relevant part of the DEM to the SAR coordinates of the specific interferogram via a *look-up table*. A look-up table contains the corresponding coordinates for every pixel of the DEM in SAR geometry.

Once the part of the DEM is transformed into SAR coordinates, a ‘topography-only’ interferogram is simulated from the transformed DEM with GAMMA’s *phase_sim* tool (within the DIFF&GEO module). For the simulation of the ‘topography-only’ interferogram, the imaging geometry of the specific, mixed ‘topography/motion’ interferogram is used. This geometry is contained in the *SLC parameter file*, the *baseline file*³ and the *offset parameter file*⁴.

After simulating a ‘topography-only’ interferogram, GAMMA’s *sub_phase* tool is used for directly subtracting the simulated ‘topography-only’ phase from the mixed ‘topography/motion’ interferogram (Figure 4.4). The spatial baseline B_{ij} of the simulated ‘topography-only’ interferogram has the same length as for the specific mixed ‘topography/motion’ interferogram. This leaves the interferometric phase which is related to surface displacement along the satellite’s LOS $\Delta\phi_{motion}$ (Figure 4.4, right-hand side).

³Baseline file: Contains information on the spatial baseline.

⁴Offset parameter file: Contains information on the interferogram size and the applied multi-looking.

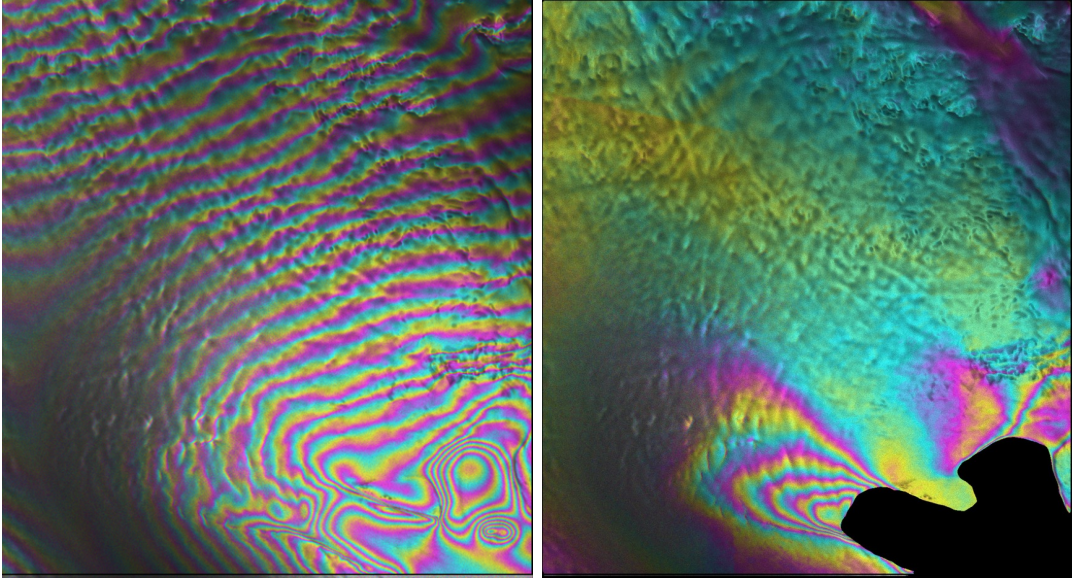


Figure 4.4.: Left: Interferogram. Fringes induced by surface displacement in the satellite’s LOS and surface topography. Right: Interferogram after subtracting a simulated ‘topography-only’ phase trend, yielding phase information which is solely related to surface displacement in the satellite’s LOS.

4.3. Phase unwrapping

After subtracting the simulated ‘topography-only’ interferogram, the displacement induced phase difference $\Delta\phi_{motion}$ is still in an ambiguous state known only as a modulo of 2π (Figure 4.5 left-hand side). The ambiguity is reached if the horizontal displacement of an area exceeds 7.24 cm or the vertical displacement exceeds 3.07 cm since the interferogram arises from surface displacement only. The procedure to solve this phase ambiguity is called *phase unwrapping*. Assuming a perfectly smooth interferogram where all fringes lie between $+\pi$ and $-\pi$, the phase can be unwrapped by integrating the phase gradients over the whole interferogram (Massom and Lubin 2006, p. 85). This approach fails at the moment when a local phase gradient $> \pi$ or $< -\pi$, primarily because of phase noise. Therefore, an adaptive filtering step is performed before the actual phase unwrapping to keep the phase noise as low as possible. In this study phase unwrapping was performed with GAMMA’s MCF (*Minimum Cost Flow*) algorithm within the ISP module. Phase unwrapping requires the most computational power in the whole processing chain. For a patch size of 1024 x 1024 pixels, GAMMA’s MCF algorithm requires approximately 320 MB of working memory (Wegmüller and Werner 2002). For comparison, some of the interferograms generated in this thesis reach sizes of 10213 x 2456 pixels. Therefore more

4. Processing chain: From four satellite scenes to a three-dimensional displacement field

than 8 GB working memory are needed, which requires a 64 bit system. Both the wrapped interferogram and the unwrapped interferogram reflect relative changes in the interferometric phase.

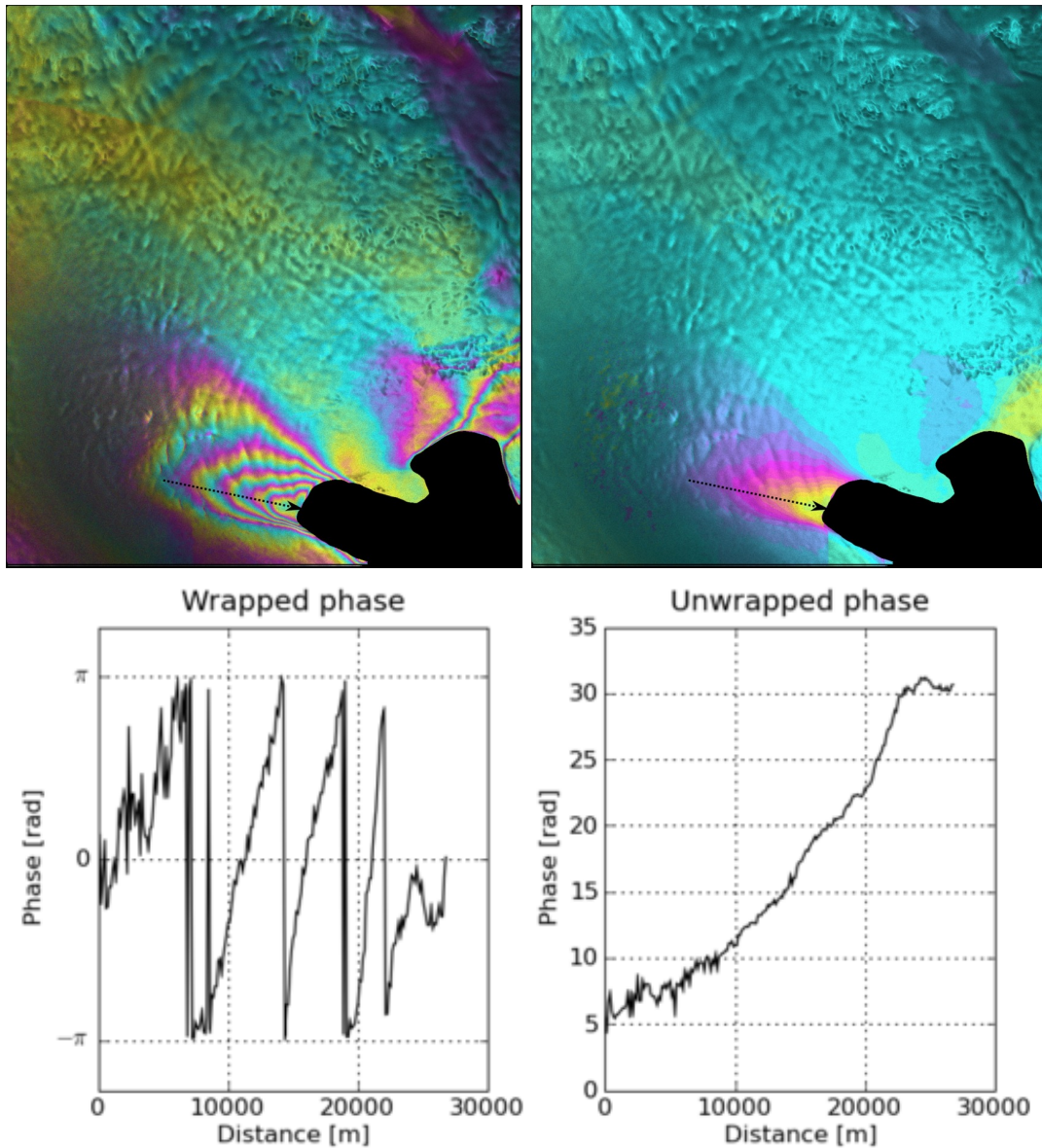


Figure 4.5.: Top left: Wrapped phase of interferogram related to surface displacement only. Top right: Same data after phase unwrapping with GAMMA's MCF algorithm. Bottom: Profiles along the dashed line in the wrapped and unwrapped interferogram.

4.4. Adjustment of unwrapped phase using Ground Control Points

After the removal of orbital and topographical fringes the phase values of the unwrapped interferogram are attributed to relative surface displacement in the satellite's LOS. The relative phase is now divided by the temporal baseline if necessary ($\Delta T = 1$ day for ERS-1/2 *Tandem Mission*; $\Delta T = 3$ days for ERS-1 *Ice Phase*).

To achieve absolute phase values, an unknown constant phase needs to be subtracted from the unwrapped interferogram (Liu et al. 2008, p. 290). This is because phase unwrapping does not create absolute values from the interferogram but generates a continuous phase with an arbitrary initial seed point. Therefore, $\Delta\phi_{motion}$ is described by

$$\Delta\phi_{motion} = \Delta\phi - \Delta\phi_0 \quad (4.1)$$

where $\Delta\phi_{motion}$ is the absolute motion-induced phase in the satellite's LOS and $\Delta\phi$ is the relative motion-induced phase in the LOS direction. The unknown phase value which needs to be subtracted is denoted as $\Delta\phi_0$.

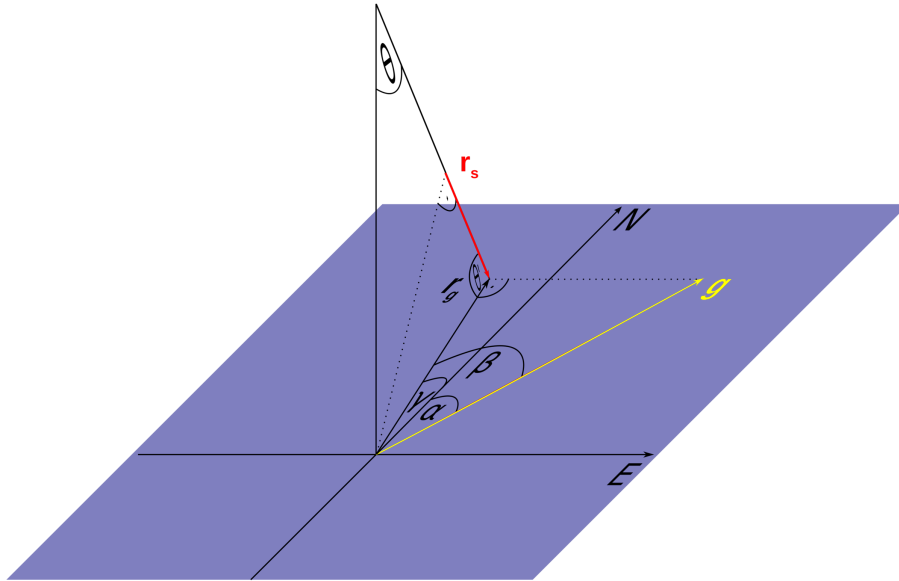


Figure 4.6.: Three-dimensional illustration of the relation between GPS-derived velocity (g , yellow) and the velocity along the satellite's LOS (r_s (slant range); r_g (ground range)). Angle θ is the satellite's look angle which is about 23° for ERS-1/2 at the scene center.

4. Processing chain: From four satellite scenes to a three-dimensional displacement field

As the whole region of interest is covered with ice, it is hard to find exposed bedrock where the ice flow is known to be zero. Such tie-points would clearly define the unknown phase offset $\Delta\phi_0$, as residual velocity around these points could be set to zero. Fortunately, sporadic GPS velocity measurements are available in the region of interest (Table 3.2). The velocity control points have a known geographic position, a known velocity in m/d and a directional angle α which is defined against the north direction. For the adjustment of the measured surface velocities, the GCPs indicated as red arrows in Figure 3.3 are used. The GCPs used for the calibration of the grounded ice were selected at a distance far enough from the grounding zone, so that tidal movement could not affect the interferometric velocity measurement. As the heading of the satellite is known from the SLC parameter file, it is possible to convert the GPS measured surface velocity into the velocity component along the satellite's LOS \mathbf{r}_s (Figure 4.6) by

$$|\mathbf{r}_s| = (\cos \beta \cdot |\mathbf{g}|) \cdot \cos \theta' \quad (4.2)$$

where β is composed of γ and α . Angle γ can be calculated by $2\pi - (\text{heading} + 1/2\pi)$ as ERS-1/2 have a right looking geometry. Angle α indicates the angle between the GPS-derived velocity vector \mathbf{g} and the true north direction and is given in Table 3.2. Angle θ' is calculated for every pixel in the unwrapped interferogram with GAMMA's *look_vector* tool (within the DIFF&GEO module). Once the velocity along the satellite's LOS is known it can be converted into a phase value (Liu et al. 2008, p. 291), representing the surface displacement at the reference point along the satellite's LOS by (see (2.15))

$$\Delta\phi_{GCP} = \frac{4\pi|\mathbf{r}_s|}{\lambda}. \quad (4.3)$$

As a result, $\Delta\phi_0$ in (4.1) can be described by

$$\Delta\phi_0 = \Delta\phi - \Delta\phi_{GCP}. \quad (4.4)$$

In order to cancel out any form of noise which may falsify the exact value, the averaged value of a 5 x 5 pixel wide window is taken into account for $\Delta\phi$. A *Python* script was written which transforms the geographical coordinates of the GCP into the geometry of the interferogram by using GAMMA's *coord_to_sarpix* tool. It automatically reports the averaged value of a 5 x 5 pixel window for $\Delta\phi$ around the coordinates of the specific GCP. The calculated phase value $\Delta\phi_{GCP}$ of the specific GCP is then subtracted from $\Delta\phi$ by (4.4). Thereafter, $\Delta\phi_0$ is subtracted from the unwrapped interferogram by another self-written *Python* application. The output of this script ends with **.unw_corr* which stands for *corrected unwrapped phase*. The corrected unwrapped interferometric phase is converted into a one-dimensional surface displacement map (Figure 4.7 right-hand side) with GAMMA's *dispmap* tool (within the DIFF&GEO module). The surface displacement along the satellite's LOS is given in meters per day. Positive values correspond to displacement towards the

4.4. Adjustment of unwrapped phase using Ground Control Points

sensor while negative values correspond to displacement away from the sensor (Wegmüller and Werner 2002).

After creating a one-dimensional displacement field (Figure 4.7 right-hand side), the data needs to be geocoded (Figure 4.8 right-hand side).

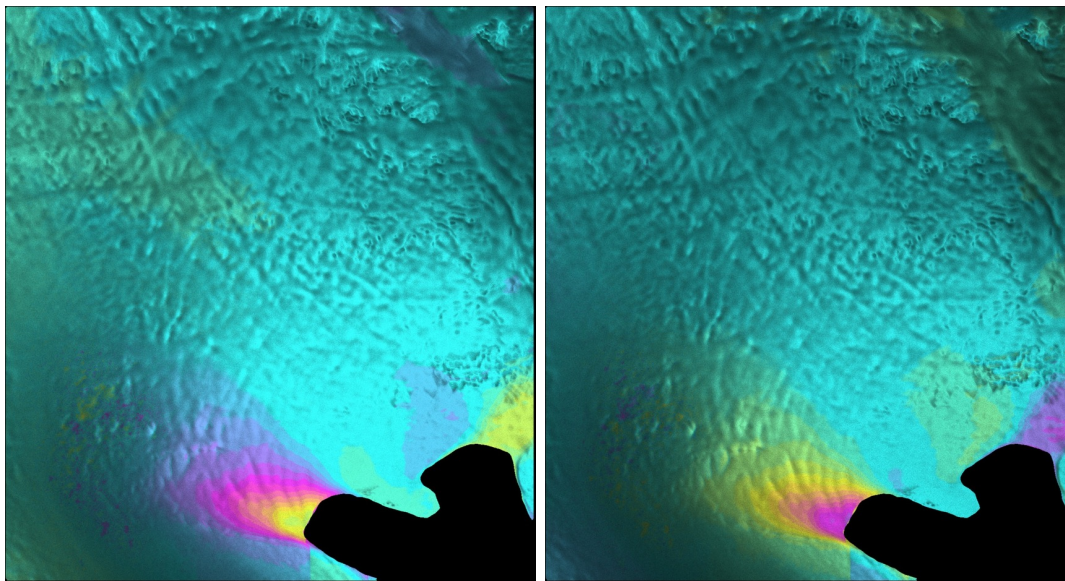


Figure 4.7.: Left: Adjusted unwrapped ‘motion-only’ interferogram. Right: The same interferogram converted into a one-dimensional displacement map, representing the surface displacement along the look vector in meters per day. Here, the red zone indicates displacement of -0.15 m/d and the cyan colored areas indicate slower displacements down to $\pm 1e-5$ m/d.

Geocoding can be described as the transformation from the geometry of the SAR sensor into a geographical coordinate system (Moll 2008, p. 50). For all geocoded data in this thesis, a polar stereographic coordinate system is used, with a true latitude of 71° south and a central meridian of 0° east, based on the WGS-84 ellipsoid as recommended by Sievers and Bennat (1989). The images in Figure 4.7 are given in SAR coordinates, with each pixel defined by its range and azimuth coordinate. For geocoding, the three-dimensional position of every pixel is needed. Therefore, the same look-up table is used that was created for the transformation of the DEM into SAR coordinates (see Chapter 4.2). The horizontal accuracy of this method is approximately within 50 m - 100 m (Moll 2008, p. 50).

4.5. Derivation of three-dimensional ice-flow using ascending and descending passes

As mentioned above, the surface displacement is only measured along the satellite's LOS. Three-dimensional displacement ice can not be described fully by one interferogram. Once two one-dimensional velocity fields of the same area are calculated, one from a descending satellite track and one from an ascending satellite track (Figure 4.8), it is possible to calculate the surface displacement in a more complete way. The two tracks are thought to represent two components of a three-dimensional velocity field. This technique is highly dependent on the geographical latitude, as the LOS of the ascending and descending satellite tracks approximate each other until they almost reach the same orientation towards surface displacement in the proximity to the equator (Moll 2008, p. 52).

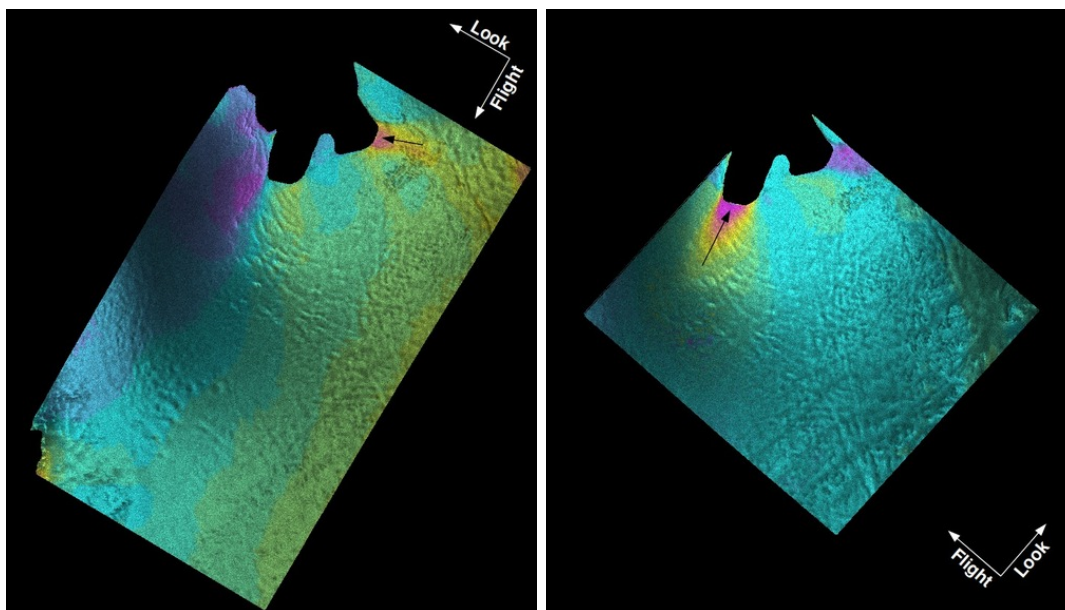


Figure 4.8.: Left: One-dimensional flow field of a descending satellite track (geocoded). Right: One-dimensional flow field of the overlapping ascending satellite track (geocoded). The white arrows indicate the LOS of the satellite and its flight direction. The black arrows represent the main ice flow which is seen by the satellite.

A cartesian three-dimensional velocity vector \mathbf{v} is given by (Joughin et al. 1998, p. 27)

$$\mathbf{v} = v_x \hat{\mathbf{x}} + v_y \hat{\mathbf{y}} + v_z \hat{\mathbf{z}} = \mathbf{v}_h + v_z \hat{\mathbf{z}} \quad (4.5)$$

4.6. Horizontal flow of the floating shelf ice

where \mathbf{v}_h represents the horizontal displacement and $v_z\hat{\mathbf{z}}$ the vertical displacement of the full three-dimensional displacement. Each LOS displacement of the ascending and descending tracks (as shown in Figure 4.8) reflects only one velocity component. Since the relation between the ascending and descending track is nonorthonormal their coordinate systems need to be rotated with respect to each other as described by Joughin et al. (1998, p. 35). Thereafter \mathbf{v}_h can be calculated. Surface parallel ice flow is assumed for the calculation of the vertical component $v_z\hat{\mathbf{z}}$ in (4.5). Therefore, the DEM is needed to calculate the terrain's surface slope. This means that the three-dimensional velocity vector \mathbf{v} is calculated from two different LOS directions and a known surface slope. Figure 4.9 shows a three-dimensional velocity field which is derived by combining the two one-dimensional velocity fields shown in Figure 4.8.

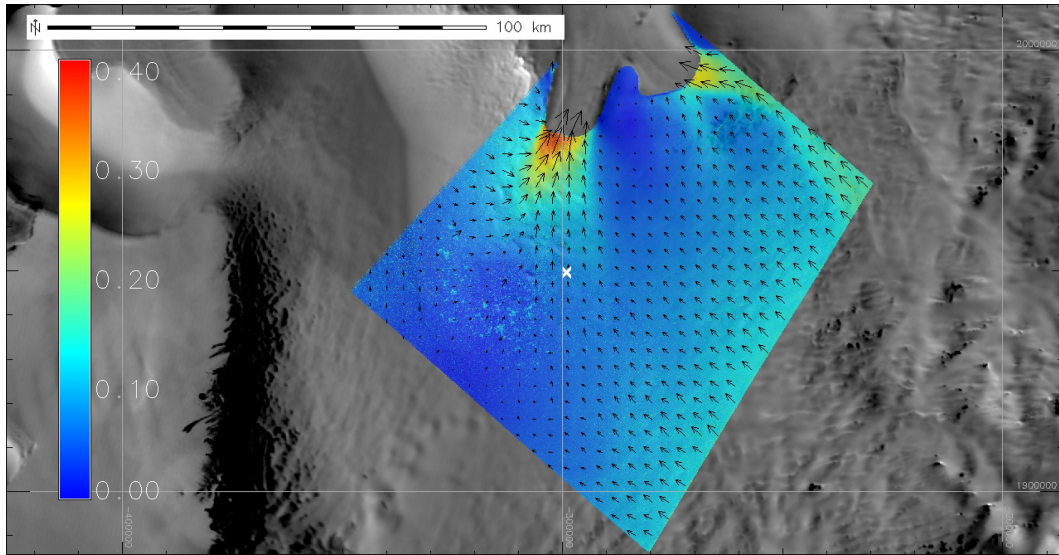


Figure 4.9.: Three-dimensional velocity field in m/d. Composed from ERS tracks 221 and 045 (Figure 4.8), the black arrows indicate the direction of flow and their lengths are proportional to velocity. The white cross marks the GCP which was used for calibrating the unwrapped phase. In the background is the NSIDC MODIS mosaic of Antarctica (MOA).

4.6. Horizontal flow of the floating shelf ice

Apart from the surface velocities of the grounded ice sheet, it was also possible to derive the three-dimensional horizontal flow of the floating shelf ice from a combination of two one-dimensional velocity fields. The floating shelf ice requires separate

4. Processing chain: From four satellite scenes to a three-dimensional displacement field

consideration, as it is affected by tidal movement. It is therefore treated without a relation to the grounded ice. To determine flow velocities of the floating shelf ice a parallel uplift/subside due to tidal movement is assumed. This can be tested by counting tidal fringes (Figure 4.3) at several positions in the grounding zone. If all fringe patterns show the same ascent (or descent), the floating part has been lifted (or lowered) symmetrically in respect to the side margins. In this case, the constant offset is removed with a GCP on the shelf ice. As the local InSAR DEM does not cover the floating shelf ice, $\Delta\phi_{topography}$ is only simulated from the Bamber DEM. However, topographical information in the unwrapped phase is not as important, since the floating shelf ice is flat except for sporadic ice rises which need to be masked out because of tidal movement.

5. Evaluation of the three-dimensional velocity fields

In this chapter, the quality of the flow velocities is tested and possible sources of error are discussed. For this purpose, overlapping regions of the three-dimensional velocity fields are compared, and the influence of external elevation data is tested by comparing three-dimensional velocity fields based on different DEMs. Furthermore, the InSAR-derived ice flow is compared with sporadic GPS velocity measurements.

5.1. Mosaicking

After the generation of several three-dimensional velocity fields (see Chapter 4) a mosaicking step is performed to get an area-wide velocity field of the ice surface. For mosaicking, a shell script was written for the open source GRASS GIS software (for a documentation of GRASS GIS see Neteler and Mitasova (2008)). The overlapping parts of the single three-dimensional velocity fields are averaged first and then stacked with the GRASS GIS *r.patch* module. This is done for the flow magnitude as well as for the flow direction α .

The result for the flow magnitude of grounded ice based on the local InSAR DEM is shown in Figure 5.1 on the left-hand side. The three-dimensional velocity of the floating ice shelf is derived by a combination of only two tracks (track 493 and track 460). Therefore no overlap needs to be averaged for the three-dimensional shelf ice flow. In addition, there is no overlap with the velocity fields of the grounded ice. This is because the horizontal movement of ice flow is superimposed by vertical movement in the grounding zone. For this reason, the horizontal movement in the grounding zone can not be derived by SAR interferometry. In Figure 5.1, the shelf ice velocities are omitted, but will be added for the final product (see Chapter 6).

The overlap of adjacent three-dimensional velocity fields enables not only stacking but also subtraction. The result of the latter is shown as a deviation map in Figure 5.1 on the right-hand side. The differences between the overlapping parts of the three-dimensional velocity fields are within the range of -0.10 to 0.20 m/d. The mean

5.1. Mosaicking

value for the differences in the overlapping regions is

$$\bar{x}_{overlap1} = 0.003 \text{ m/d} \quad (5.1)$$

for region 1 (Figure 5.1 right-hand side) and

$$\bar{x}_{overlap2} = 0.098 \text{ m/d} \quad (5.2)$$

for region 2. Looking at the magnitude of single velocity fields, the results seem reasonable in most cases. Errors only become apparent after mosaicking or subtracting at least two three-dimensional velocity fields. The relative errors can be great especially in slow moving areas. Potential sources of errors and possible solutions are discussed in the next section.

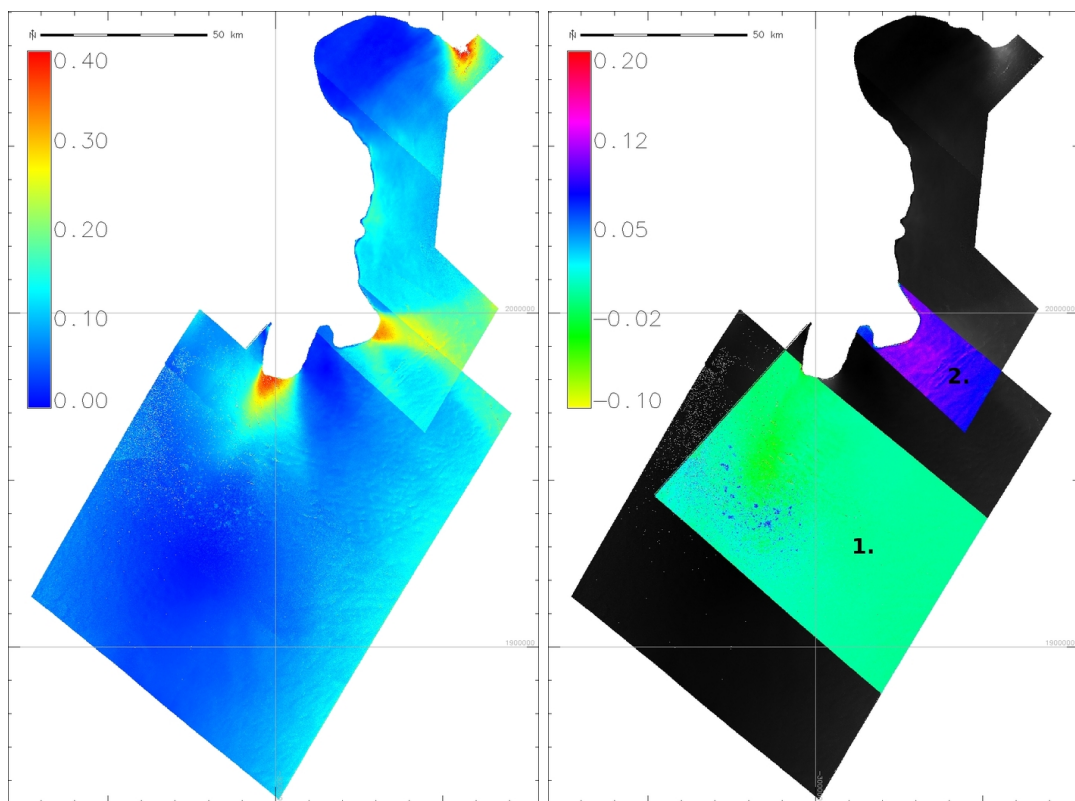


Figure 5.1.: Left: Mosaic of three-dimensional flow velocities of grounded ice. The flow velocities are based on the local InSAR DEM. Right: Absolute differences in the overlapping areas for the same data. The flow velocities in m/d are color coded in each panel as indicated by the numerical scales.

5.2. Processing uncertainties

The errors observed during the mosaicking process may be caused by a number of reasons. The most important errors are explained in the following section and possible solutions are suggested. Figure 5.2 shows the differences between the adjacent three-dimensional combinations of track 221 with track 045 and track 178 with track 045 (see Figure 3.1 and Table 3.1 for exact location) in flow direction α in $^\circ$, as well as the differences in flow magnitude in m/d. All unwrapped ‘motion-only’ interferograms in this example were calibrated with the same GCP (red cross in the upper images of Figure 5.2 and black dot in the profiles at the bottom). The error is close to zero at the position of the GCP but increases nearly linearly over the whole overlap (upper profile in Figure 5.2). Such a systematic error suggests uncertainties in the processing. The deviations in velocity are also visible in the unwrapped phase. Since track 045 is used for both three-dimensional combinations, either track 178 or track 221 show a linear trend which is referred to as *differential phase ramp*. Differential phase ramps may originate from an imprecise baseline model. Estimates of the spatial baseline B_{ij} from precision orbit ephemeris data are only accurate to within tens of centimeters (Massom and Lubin 2006, p. 62). This can introduce significant residual errors in motion mapping. According to Joughin et al. (1996, p. 564) an error of 1 m in B_{ij} can lead to a velocity error of about 39 m/a. In principle, $\Delta\phi_{motion}$ is completely independent from the spatial baseline, but B_{ij} is needed for the simulation of the ‘topography-only’ interferogram (Chapter 4.2). It was therefore attempted to eradicate baseline uncertainties as described in the following. The typical approach for InSAR elevation mapping is to refine the baseline with elevation GCPs as described by Drews et al. (2009, p. 2). However, for motion mapping this is not directly possible, as the unwrapped mixed ‘topography/motion’ interferogram is not necessarily equal to a pure elevation GCP. Therefore it was tried to apply this method only in areas where motion seemed negligible. The baseline refinement uses laser altimetry measurements from ICESat’s GLAS as a reference base. ICESat’s laser altimeter provides elevation tie points every 170 m along the ICESat track. GAMMA’s *base-ls* tool (within the ISP module) is used to adjust B_{ij} with these external elevation tie points. The *base-ls* tool is able to compute a more precise estimate of the interferometric baseline. Therefore the ICESat GCPs were converted into the geometry of the specific interferogram and the corresponding unwrapped interferometric phase (of the mixed ‘topography-motion’ interferogram) was extracted at these points with GAMMA’s *gcp_phase* tool. The ICESat GCPs were selected in areas where the ice flow is assumed to be negligible (for example a.) in Figure 4.3) in the mixed ‘motion-topography’ interferogram. The *base-ls* tool uses a least-squares algorithm to determine the baseline parameter values from these tie points. At each point along the specific SAR track B_{ij} is recalculated by *base-ls* (Wegmüller and Werner 2002). However, this approach does not yield a better result in this example.

5.2. Processing uncertainties

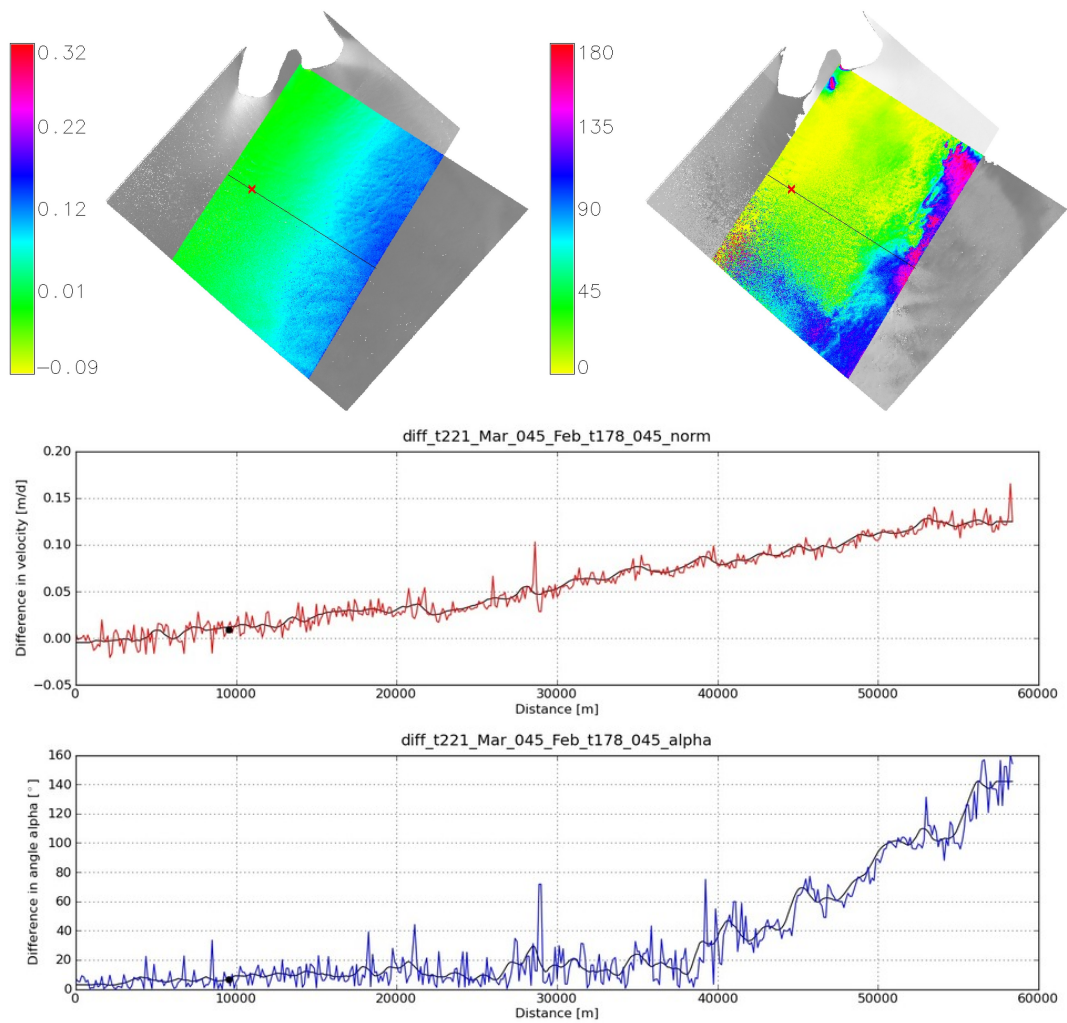


Figure 5.2.: Differences between two three-dimensional flow fields in the overlapping region. Top left: Difference in velocity in between 3-D combination (track 221, track 045)-(track 178, track 045). Top right: Difference in flow direction α for the same data. The color code indicates the differences in velocity in m/d and in flow direction in $^\circ$, respectively. Bottom: Profile along the black line in the difference plots of velocity and direction. The black dot in the profiles and the red cross in the upper images represent the GCP which was used for the adjustment of the unwrapped phase.

In general, B_{ij} should be as small as possible for ice motion mapping in order to minimize residual topography related errors (Massom and Lubin 2006, p. 71). On the other hand, B_{ij} should be as large as possible for topographical mapping to decrease the altitude of ambiguity. However, due to the limited data availability, it is usually not possible to chose between different baselines.

Also, residual phase ramps can originate from the SAR processing. Drews et al. (2009) tested different SAR processors and the results (DEMs in this case) deviated significantly from each other. The deviations were tracked down to the SAR processing history. Differences can even occur when the same SAR processor is used, since some parameters are estimated by the SAR processor for every frame individually (e.g. the Doppler centroid) (Drews et al. 2009, p. 5). In such a case, however, the user is almost helpless.

Apart from an inaccurate baseline model and uncertainties in the SAR processing, errors can further originate from other reasons and their combinations. For example, areas with low coherence should be excluded for motion mapping. This is why in the most eastern part of the final three-dimensional velocity field (Figure 6.2), next to the summit of Halvfarryggen, a relatively large area was masked out. In this area, high accumulation rates were observed by Rotschky et al. (2007), which often leads to a bad coherence between SLC images acquired at different times, a process referred to as temporal decorrelation (see Chapter 2.3). Also, atmospheric contribution may be an underestimated source of error. Further problems may arise from inaccurate co-registration, errors during phase unwrapping (in general because of phase noise, see Chapter 4.3) and inaccuracy of the DEM used (see Chapter 5.3). In conclusion, a global fit, where all combinations of errors are set to a minimum, would be very valuable.

A polynomial fit seems a promising approach. However, a reference base is needed on which the polynomial fit can be based. This is a major challenge as GPS-derived flow measurements are rare (see Chapter 3.3) and control points ideally need to be distributed evenly over the region of interest for such an approach. An idea is to derive additional velocity information via speckle or feature tracking. Both approaches track individual characteristics in a satellite image. Features, for example, are tracked in an optical image, speckle (intensity) in a radar image (for further explanation, see, for example, Massom and Lubin (2006, p. 101 ff.)). As the ice moves slowly over flat terrain in the region of interest, it is hard to find crevasses which could be tracked. Therefore, a feature tracking approach is not a promising option here. The advantage of speckle tracking is that the coherence of the radar scenes do not need to be as high as for an InSAR approach. However, the resulting velocity field would be of low quality compared to an InSAR-derived velocity field. Implementing speckle tracking may be promising for future studies but is beyond the scope of this thesis.

Sometimes it is possible to locate flow lines in the backscattered radar signal to which the directional component of the derived flow velocity can be aligned (Joughin et al. 1998, p. 27); unfortunately, this is not the case here. A similar approach is based on the idea that ice flows downhill (as a first order assumption).

5.2. Processing uncertainties

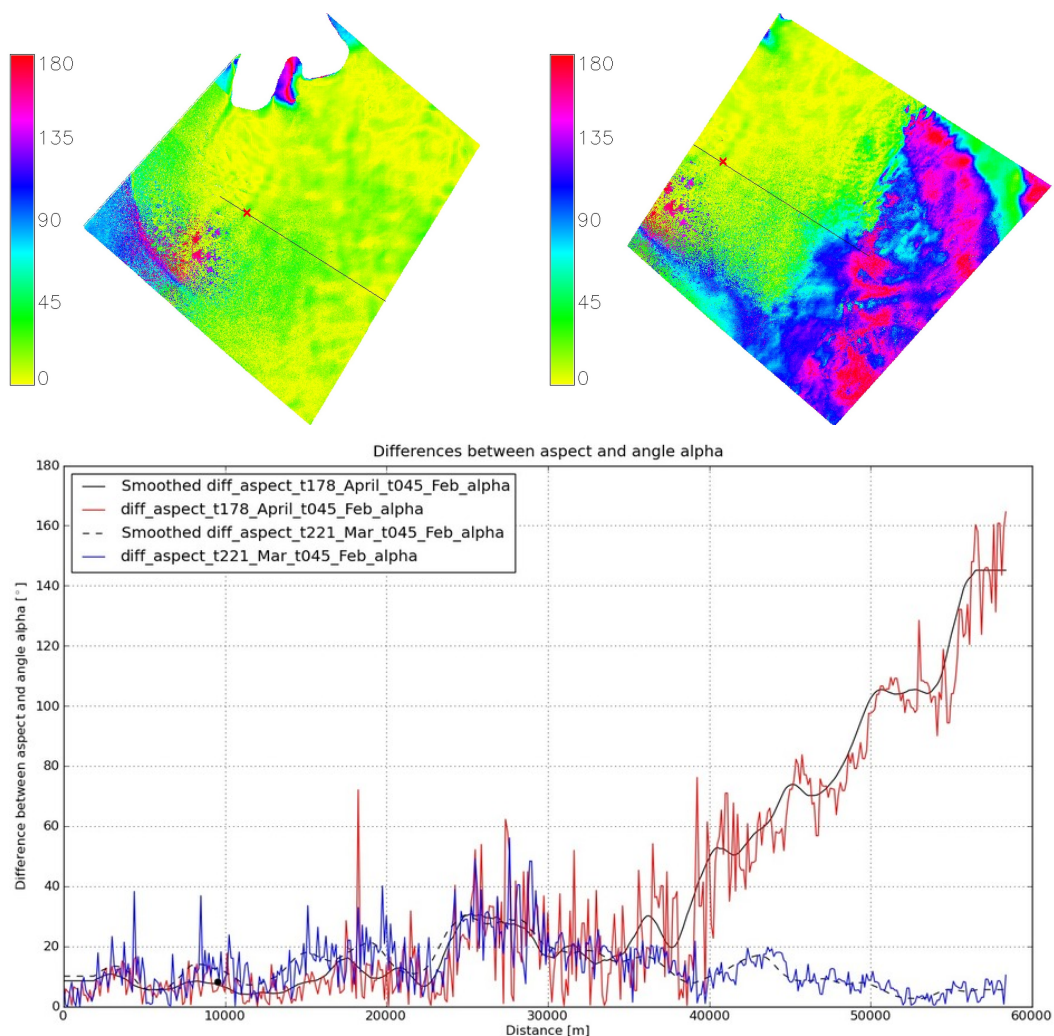


Figure 5.3.: Differences between aspect angle and flow direction α . Top left: Difference between aspect angle and α from track combination 221 and 045 in $^{\circ}$. Top right: Difference between aspect angle and α from track combination 178 and 045 in $^{\circ}$. Bottom: Profile along the black line in the overlapping part of both flow fields. The black dot in the profiles and the red cross in the upper images represent the GCP which was used for the adjustment of the unwrapped phase. The flow direction of the three-dimensional velocity field generated by combining track 221 with track 045 corresponds much more with the aspect direction than the track combination of track 178 with track 045.

The main idea in such an approach is to adjust the flow magnitude by minimizing the difference between the flow direction α and the aspect direction. Such a minimizing procedure includes formulating the deviation from the downhill direction as a cost function which must be minimized. The idea is to vary the X and Y components

individually to find the best large scale fit. However, this approach does not always converge and further constraints on the flow magnitude may be necessary. Due to the limited time available for this thesis it was not possible to fully implement and test this approach.

In a first attempt, slope, aspect, flow direction and flow magnitude were calculated for the local InSAR DEM. The DEM was resampled on a 500 m x 500 m grid to smooth the surface for calculating the topographical parameters slope and aspect. The aspect and slope map was calculated with Envi 4.4. Envi offers a more accurate algorithm for calculating aspect directions than other GIS software (e.g. ArcGIS, GRASS GIS), as the kernel size can be defined by the user. The standard value in most GIS applications is a 3x3 window which leads to 8 cardinal points, each representing 45° to the next cardinal point. Using a kernel size of 10, the aspect angle can be calculated with a much higher accuracy. Envi generates an aspect angle where 0° represents the north direction and angles increase clockwise (ITT 2002). The direction of the derived three-dimensional surface velocities was translated into the same coordinate system as the aspect generated from the Envi topography tools. Figure 5.3 shows the deviation of the three-dimensional track combinations shown in Figure 5.2 (track combination 221, 045 and track combination 178, 045) from the aspect direction. The deviation from the aspect direction is relatively small for track combination 221, 045 but larger for track combination 178, 045.

Minimizing the difference between α and the aspect angle for track combination 178, 045 leads to a more reasonable flow direction. However, the X or Y component of the flow vector is overestimated in most cases. Such a minimizing routine should be handled with care as ice does not always follow the slope gradient and aspect direction.

Figure 5.4 shows a reasonable InSAR-derived flow direction and magnitude for the main outflow glaciers into the Ekströmsen as blue arrows and the aspect direction and slope gradient as red arrows. The main ice flow does not follow the steepest slope gradient because of local longitudinal and lateral stresses. In this region, the flow of ice is probably controlled by the bed rock. In this region, ice coming from different directions accumulates and drives the main outflow into the Ekströmsen.

In conclusion, no satisfactory solution could be found for track combination 178, 045 which is why this three-dimensional combination is excluded from the final velocity field (Chapter 6).

5.3. Dependency of DEM accuracy on three-dimensional surface velocities

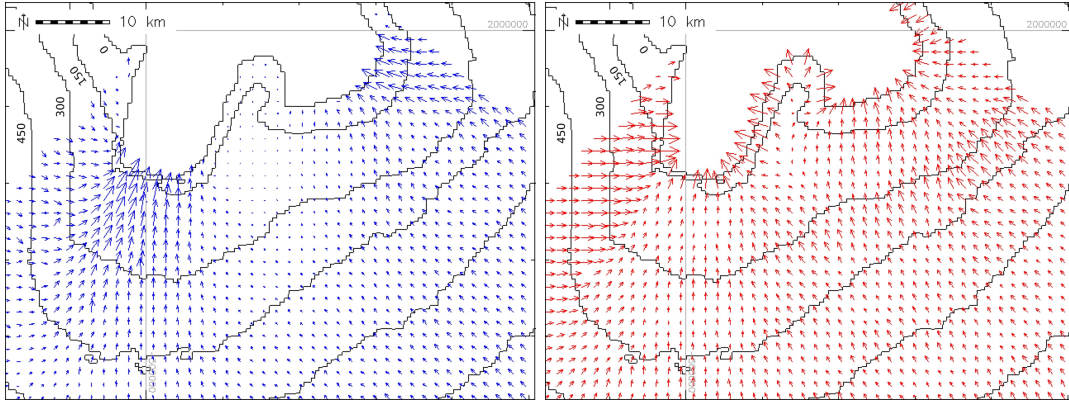


Figure 5.4.: Left: Blue arrows indicate the calculated flow direction and their length is proportional to velocity. Right: Red arrows indicate the direction of the downhill slope and their length is proportional to the slope gradient.

5.3. Dependency of DEM accuracy on three-dimensional surface velocities

In Chapter 3.2 the available elevation models for the region of interest have been compared with airborne laser altimetry data and kinematic GPS measurements. A high RMSE was calculated for some of the evaluated DEMs. Therefore, the currently most accurate Antarctic-wide DEM (Bamber DEM) and the most accurate local DEM (local InSAR DEM) have been chosen for simulating ‘topography-only’ interferograms and subtracting these from the specific mixed ‘topography-motion’ interferograms. All track combinations shown in Table 6.1 have been generated this way and have been mosaicked as described above. Figure 5.5 (top) shows the absolute differences in m/d between the calculated three-dimensional velocity fields based on both DEMs. Currently, the Bamber DEM is the most widely used DEM for large parts of Antarctica. Therefore, surface velocities in other parts of the Antarctic continent have to be calculated by simulating a ‘topography-only’ interferogram from this elevation dataset. Even though the Bamber DEM is an accurate DEM on a wider scale, deviations are high in some locations.

In Chapter 3.2 both DEMs were compared to ground truth data along two profiles. Along these profiles the local InSAR DEM deviates less than the Bamber DEM. Taking profiles along these lines in the three-dimensional velocity fields shows the influence of the DEM accuracy on the flow field generation.

5. Evaluation of the three-dimensional velocity fields

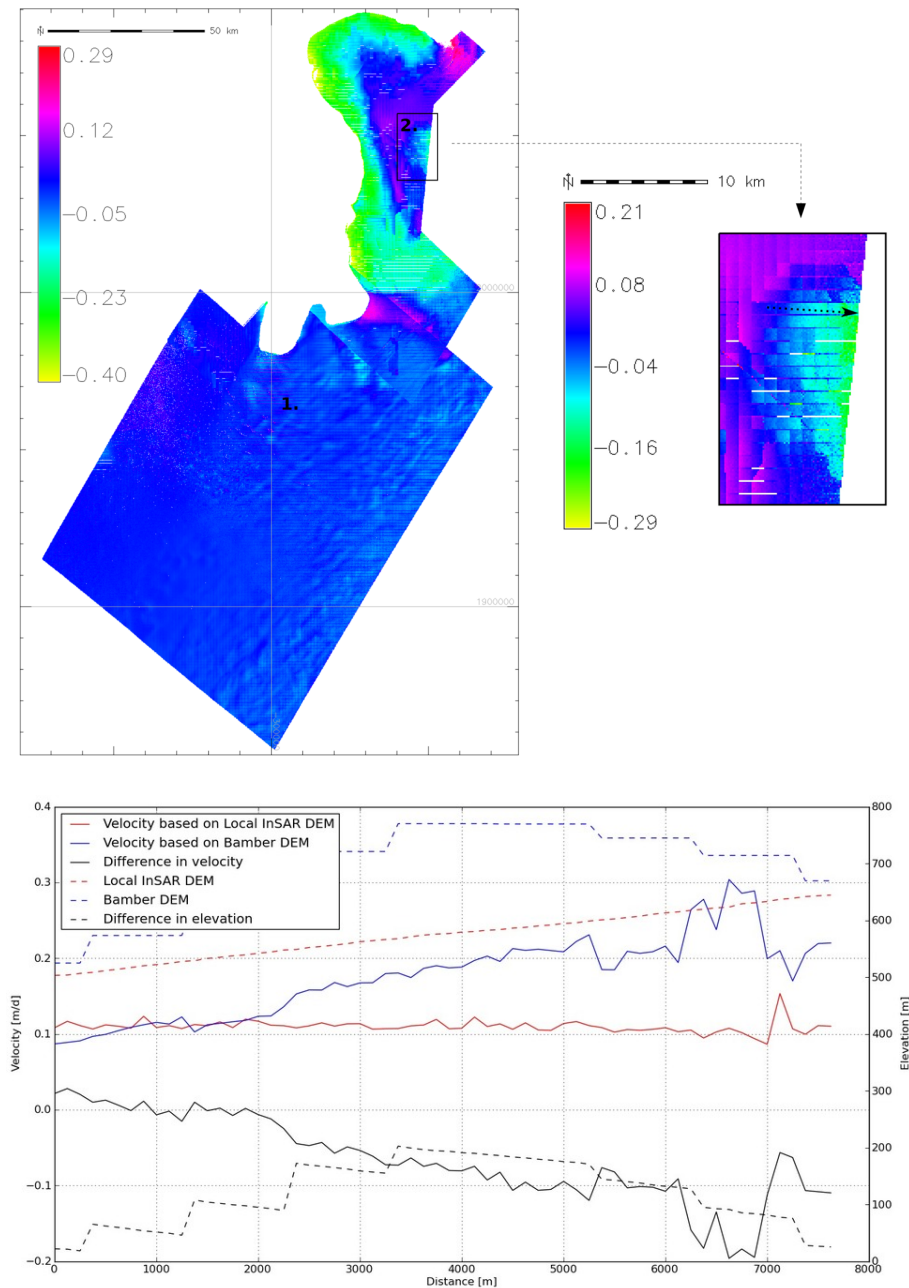


Figure 5.5.: Comparison between surface velocities based on different DEMs. Top: Differences between surface velocities based on the local InSAR DEM and the Bamber DEM in m/d. Profile 2 (Figure 3.3) is used for comparison of the generated flow velocities (dotted line in upper image). In this area, differences of up to ~ 200 m between both DEMs have been found (Chapter 3.2), which is also reflected in the generated flow velocities. Bottom: Differences in surface velocity calculated using various DEMs along dashed black line in the upper image.

5.3. Dependency of DEM accuracy on three-dimensional surface velocities

The profiles taken in Chapter 3.2 show a smaller deviation in elevation in the region denoted as 1 in Figure 5.5 compared to ground truth data than in region 2. This is reflected clearly in Figure 5.5, where the deviation in ice flow south of the Ekströmsisen (location 1 in Figure 5.5) is close to zero, while the three-dimensional velocity fields deviate up to 200% next to the summit of Halvfarryggen (Figure 5.5 bottom). This fact makes it clear that relatively small errors in slope determination can have a disproportionally large effect on velocity calculations. The uncertainties in the DEMs clearly contribute to the deviations in results presented in Figure 5.5. According to Mohr et al. (1998, p. 276) 1° uncertainty in slope is translated into a relative velocity uncertainty of $\sim 4\%$, a deviation approximately valid for this example.

The profile shown in Figure 5.5 (bottom) shows the deviation in velocity based on both DEMs in m/d as well as the deviation in elevation between both DEMs in [m] along the profile. It shows that the final product is strongly controlled by the external elevation dataset used. It is therefore highly recommended to test the quality of external elevation data beforehand.

5.4. Comparison of calculated three-dimensional velocity field with ground truth data

In this section the mosaicked velocity field based on the local InSAR DEM is compared with the available ground truth data introduced in Chapter 3.3. Most of the GPS measurements are located on the floating shelf ice and in the grounding zone, as the main geodetic goal of the field survey was to measure the response of the ice body to the ocean tides (Riedel et al. 1999, p. 239). Nevertheless, some GPS measurements were acquired on the grounded ice sheet (Figure 5.6) as well. Again, these measurements are very valuable for the validation and adjustment of the generated velocity field as no *nunataks*¹ (here the surface displacement can assumed to be zero) can be detected in the region of interest.

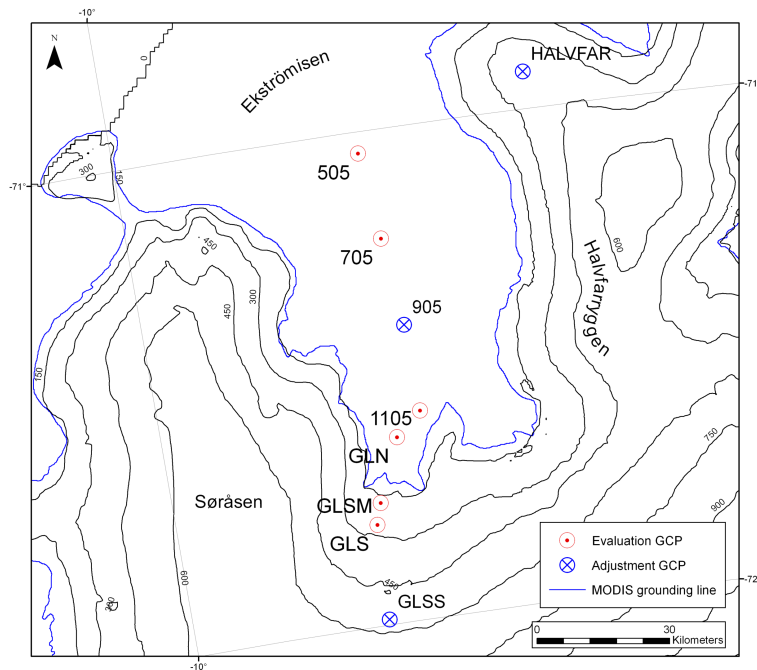


Figure 5.6.: Location of GCPs used for adjustment and evaluation of the calculated velocity field. Contour lines are located every 150 m and were derived from the local InSAR DEM, the Bamber DEM and (where available) from Landsat photoclinoetry data (unpublished data: NASA's Goddard Space Flight Center).

As the interferograms at location *GLSS* and *HALVFAR* (Figure 5.6 (blue crosses), GCP *HALVFAR* pers. comm. C. Wesche) are most likely not affected by tidal movement (see Chapter 6.1) these GCPs are used as seed points to resolve the unknown

¹Nunatak: Exposed ice free bed rock.

5.4. Comparison of calculated three-dimensional velocity field with ground truth data

phase offset from phase unwrapping (Chapter 4.4). Therefore the unwrapped phase of the combined ‘motion-only’ interferograms is either set to the X or Y component of the specific GCP. GCP *905* is used in the same way to adjust the horizontal surface displacement of the floating shelf ice, since it is located almost in the center of the combined satellite frames of track 493 and 002 (Figure 3.1).

As a result, these GCPs can not be used for an independent validation of the generated velocity field. It is thus difficult to validate the data in these regions, as no independent GPS measurements exist here.

A comparison of the GPS measurements which are not used for the adjustment of the generated velocity field and the InSAR-derived velocities is summarized in Table 5.1. The *Radar mean* value in Table 5.1 represents the averaged value of a 2 km wide area in the generated velocity field around the specific GCP. As the mean value does not deviate much from the exact pixel value (*Radar* in Table 5.1), the exact value is used for the comparison with the ground truth data (*GPS* in Table 5.1). As already mentioned by Mohr et al. (1998, p. 275), who used the same interferometric approach for measuring surface velocities in north eastern Greenland, the magnitude of the generated flow velocities often deviates more than the directional component when compared with GPS measurement. For example the flow magnitude of the

Table 5.1.: Comparison of calculated flow velocities with GPS measurements. Locations of GPS measurements are mapped in Figure 5.6

Station	Flow magnitude [m/d]				Flow direction [°]		
	Radar	Radar mean	GPS	Radar-GPS	Radar	GPS	Radar-GPS
505	0.483173	0.483703	0.457534	0.025639	326.3	337.4	-11.1
705	0.411449	0.413455	0.458904	-0.047454	335.5	351.6	-16.1
1105	0.316106	0.316735	0.398630	-0.082524	19.4	22.3	-2.9
GLN	0.321247	0.319049	0.405479	-0.084232	22.8	25.7	-2.9
GLSM	0.300128	0.292148	0.342466	-0.042337	18.3	27	-8.7
GLS	0.207898	0.207142	0.205479	0.00242	17.1	21.2	-4.1

InSAR-derived surface velocity deviates by 20.8% from the GPS measured flow magnitude at location *1105*. However, the difference in flow direction is only 11.3% at this location. This error might be due to tidal movement in this region. The opposite is found at GPS location *GLS* where the difference in flow magnitude is only 1.2%. The GPS velocity measurements (except GCP *HALVFAR*) used for adjustment and comparison were acquired in austral summer 1996/1997, around the same time that the data acquisition from ERS-1/2 took place. Consequently, an actual change of flow between times of data acquisition can be neglected in most cases.

Several profiles were taken in the regions of the main ice flow. The location of the profiles is indicated in Figure 5.7. Except for profile 2 (Figure 5.8), all profiles are shown in the Appendix. Profile 2 connects the GPS measured ground truth data (Figure 5.8). It shows the generated velocity in m/d and the change in elevation in m along the profile.

5. Evaluation of the three-dimensional velocity fields

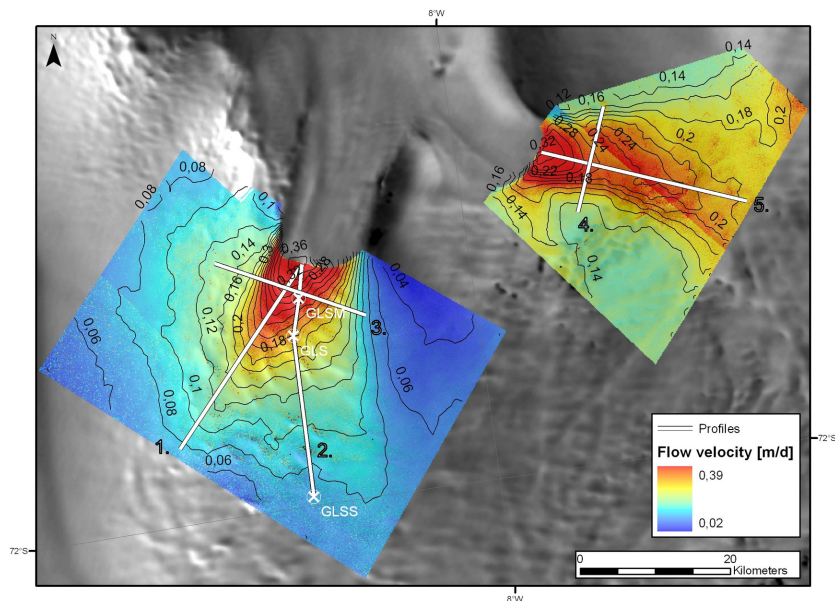


Figure 5.7.: Location of profiles in the region of two ice streams. Profile 2 follows the GPS measured flow velocities. Black lines indicate lines of equal flow velocity in m/d. In the background is the NSIDC MODIS mosaic of Antarctica (MOA).

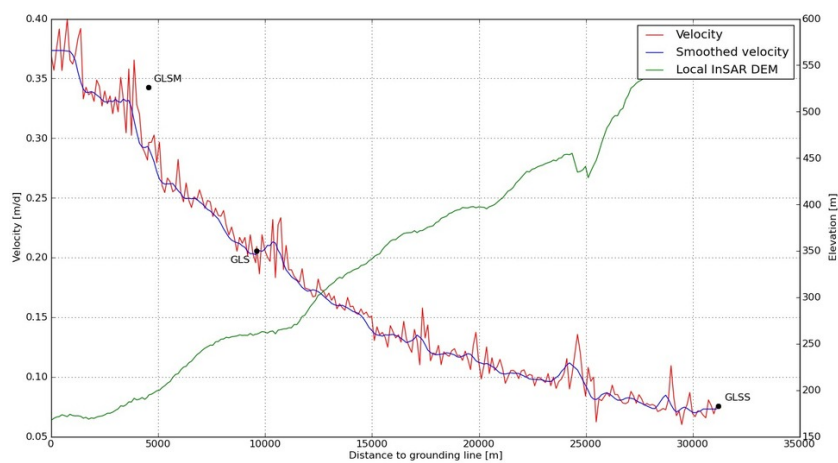


Figure 5.8.: Profile 2 as shown in Figure 5.7. Black dots indicate the GCPs used for adjustment (*GLSS*) and comparison (*GLSM*). The flow velocity fits very well to the GCPs. The highest deviation can be found near location *GLSM*, where tidal movement might be the reason for the deviation as it is located near to the grounding line. The elevation along the profile is also shown.

5.4. Comparison of calculated three-dimensional velocity field with ground truth data

The results in this example seem reasonable. The deviation of the calculated ice flow near GCP *GLSM* might be related to tidal movement in the vicinity of the grounding line. As one can see, the velocity increases towards the grounding line. Further inland, the maximum in velocity corresponds to the maximum in slope, while in the vicinity to the grounding line other driving forces might be activated, e.g. basal slip mechanisms.

6. Geophysical results

In this chapter, the final geophysical results are presented. Firstly, a precise estimate of the grounding zone location in the region of interest is given. Secondly, the calculated area-wide three-dimensional velocity field is presented. The data presented here is also available on the appended CD-ROM.

6.1. Grounding zone location

In Chapter 1.3, the grounding zone was defined as the region which separates the grounded ice sheet from the floating ice shelf. As mentioned in Chapter 1.3 locating the grounding zone correctly is necessary for several studies, including mass balance studies and ice sheet/ocean modeling.

Figure 6.1 shows the wrapped ‘motion-only’ interferogram of track 493. As the topographical part of the interferogram has already been removed, the fringes are only related to surface displacement. No unwrapping has been applied, so the phase difference is only known between $-\pi$ and π . As mentioned above, ERS SAR interferometry has a great sensitivity towards vertical displacement along the satellite’s LOS. As a result, tidal movement between the dates of data acquisition is reflected in the interferogram by a high phase gradient. It is possible to relate the grounding zone to the dense fringe pattern caused by the tidal movement (Figure 6.1). In Figure 6.1, the InSAR-derived grounding zone is compared to grounding lines derived from data from two different satellite sensors. The green line represents the grounding line extracted in the present thesis from the *Landsat Image Mosaic of Antarctica* (LIMA). The LIMA dataset is available to the public and can be downloaded from the *U.S. Geological Survey* (USGS). The pink line indicates the MODIS grounding line. The MODIS grounding line is available to the public and can be downloaded from the NSIDC. Both the MODIS grounding line and the Landsat grounding line were identified from the break in slope between steeper grounded ice and flat shelf ice. As Figure 6.1 shows, the grounding lines diverge in some places (for example in the southwestern part of the map) and do not cover the InSAR-derived grounding zone properly. However, in other places a relatively good agreement is observed.

6.1. Grounding zone location

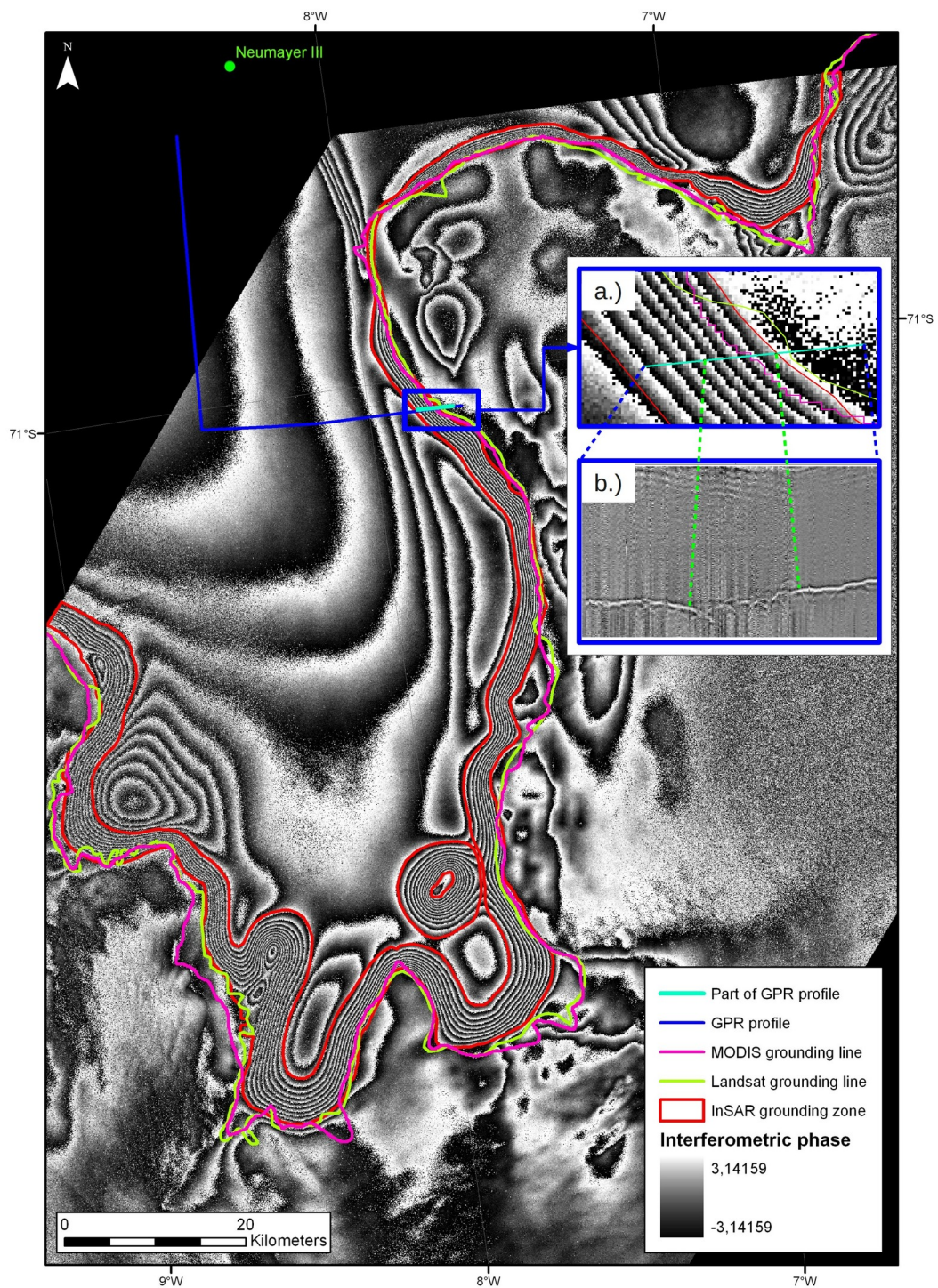


Figure 6.1.: Grounding line detection from different satellite sensors. In the background is the wrapped 'motion-only' interferogram of ERS track 493.

In order to validate the precision of the interferometry-derived grounding zone, the data was compared with a *Ground Penetrating Radar* (GPR) profile which was acquired in austral summer 2009/2010 during the LIMPICS *ANT-Land* campaign (shown as b.) in Figure 6.1). With a GPR it is possible to image the internal structure of the upper hundreds of meters of ice by recording the TWT of the transmitted radar pulse. The bedrock beneath the grounded ice and the water beneath the floating shelf ice are the strongest reflectors in the GPR data. The grounding zone can be detected easily in GPR profiles since no continuous reflector is present in this area due to strongly crevassed ice (hyperbolas between the dashed green lines in Figure 6.1).

The whole GPR profile is shown as blue line in Figure 6.1. The cyan colored line indicates the length of the radargram shown in b.). The actual grounding zone is shown as the area between the dashed green lines in the radargram. It is apparent, that the grounding zone derived by SAR interferometry is very accurate in this region.

6.2. Ice flow in the Neumayer III hinterland

In this section, the final map of surface velocities in the hinterland of the German overwintering station Neumayer III is presented. The surface velocity of the grounded ice is based on the local InSAR DEM, while the surface velocity of the floating shelf ice is based on the Antarctic-wide Bamber DEM. This is because no InSAR-derived DEM is available for this region. However, since the shelf ice is relatively flat, changes in surface elevation are negligible.

According to Hambrey and Alean (2004, p. 92) the velocity of the nonchanneled, slow moving part of the ice sheet covering West Dronning Maud Land is given with 1-15 m/a, which is also valid for parts of the map presented. Nevertheless, the channeled outlet glaciers reach velocities of up to 146 m/a, while on the floating shelf ice velocities of more than 180 m/a are calculated.

The three-dimensional track combinations used for the final geophysical product (Figure 6.2) are listed in Table 6.1.

Table 6.1.: Track combinations of three-dimensional velocity fields used for the final mosaic. The location of the tracks used is shown in Figure 3.1 and can be assigned to the IDs listed here.

(ID) Master + Slave	(Track number) Master + Slave	(Date of image acquisition) Master + Slave
1 + 9	493 + 460	18/19 Feb 1996 + 22/23 Mar 1996
2 + 6	221 + 045	05/06 Mar 1996 + 22/23 Feb 1996
2 + 5	221 + 031	05/06 Mar 1996 + 06/09 Mar 1994 (2nd Ice Phase)
1 + 7	493 + 002	15/16 Jan 1996 + 22/23 Mar 1996

6.2. Ice flow in the Neumayer III hinterland

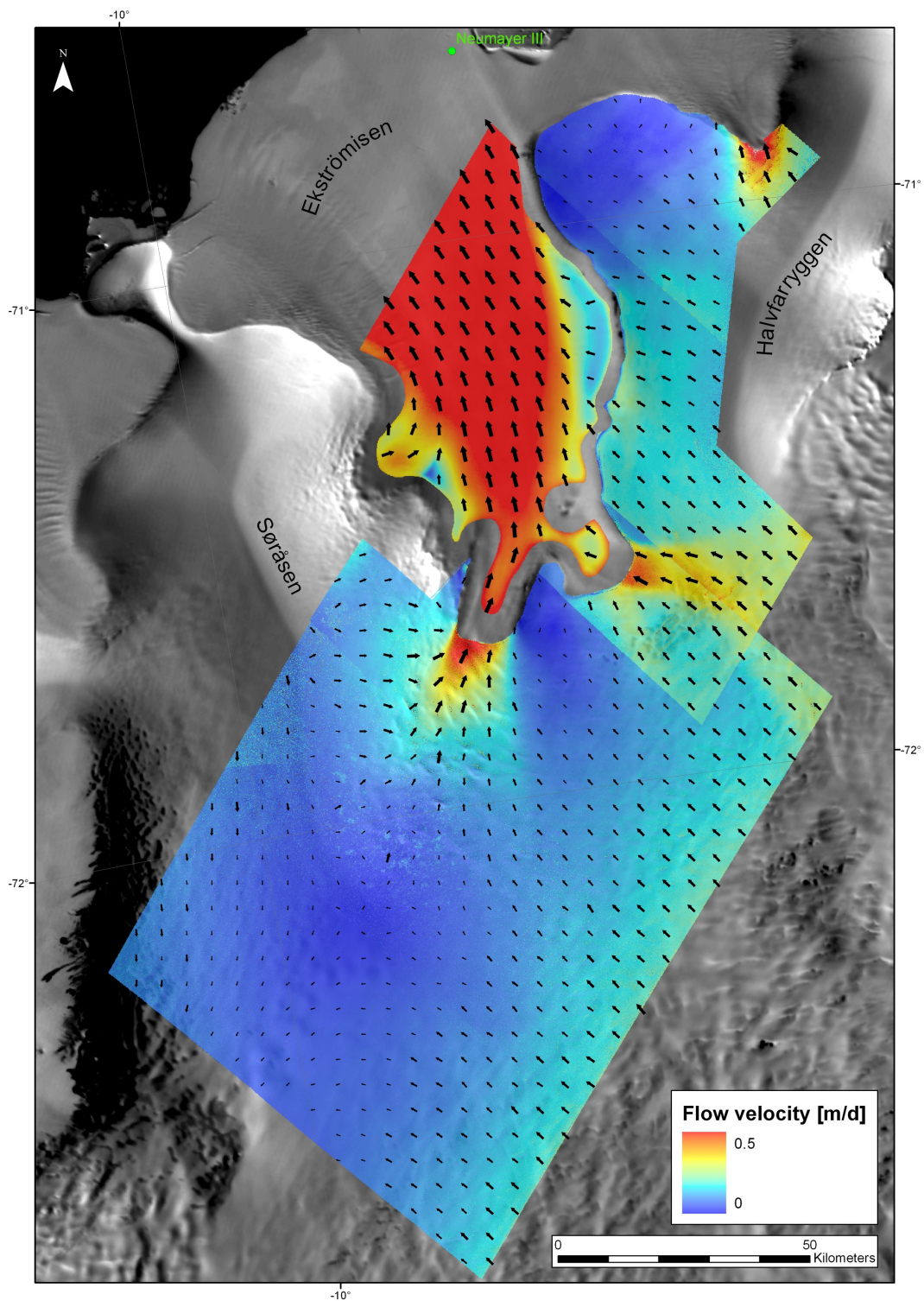


Figure 6.2.: Surface velocities in the hinterland of the German overwintering station Neumayer III in m/d. The black arrows indicate the direction of ice flow and their size is proportional to velocity. The NSIDC MODIS mosaic of Antarctica (MOA) is in the background.

7. Summary and outlook

In this thesis the ice flow in the hinterland of the German overwintering station Neumayer III has been calculated from ERS-1/2 SAR data using SAR interferometry. Apart from an area-wide velocity field, it was possible to extract the grounding zone in the region of interest.

SAR interferometry appears to be a good method for the derivation of area-wide surface velocities, but is rather dependent on accurate external data, such as digital elevation data and groundtruth data. The comparison with GPS measurements confirms that the map of surface velocities is of relatively great accuracy. The derived surface velocities vary between 0 m/d – 0.5 m/d with a locally varying error between 0.002 m/d – 0.08 m/d. However, the limitation of the GPS-derived velocity measurements used for adjustment and comparison of the calculated velocity field restricts the possibility to determine the degree of precision for the whole region of interest. The InSAR-derived grounding zone is in good agreement with the grounding zone evaluated from a GPR profile.

Although the ERS datasets are relatively old, they are still one of the best data sources for mapping ice motion on a wider scale. However, one has to keep in mind that the final results only reflect the surface velocities between 1994-1996.

In order to obtain better results, additional ground truth data is needed to adjust and evaluate the calculated velocity field more precisely. If these are not available, other ways to refine the calculated velocity field need to be found. Therefore, possible sources of errors which may lead to imprecise flow velocities have been discussed. The main error is believed to originate from an imprecise baseline model. Other potential errors may arise from the raw data or external parameters. After a refinement of the calculated flow velocities, a comparison with measurements of present day ice flow would be a promising approach in order to determine possible changes in ice flow between 1997 and today. Also, the final map of surface velocities could be used for mass flux calculations when combined with an ice thickness model of the region. However, since the InSAR technique presented in this thesis only permits measurement of the displacement of the upper layers of ice, additional information about the internal ice flow is required.

A. Appendix

A.1. Automation of the processing chain

In order to automate the long chain of commands needed for the whole interferometric processing the top-level script *3D_DISP.py*¹ (Figure A.1) was written in the programming language *Python*. A *SLC_list* and different processing parameter files need to be created manually by the user to run *3D_DISP.py*.

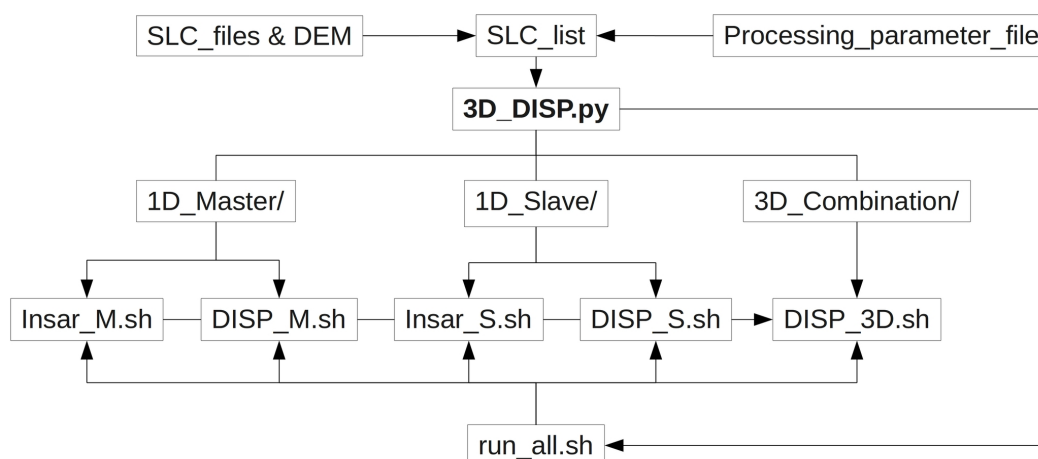


Figure A.1.: Basic structure of the Python script *3D_DISP.py* which was written to automate the generation of three-dimensional velocity fields.

The *SLC_list* contains information where the SLC images, the currently used DEM, and the processing parameter files of each SLC image pair are stored. The processing parameter files contain information of initial offsets between the SLC images, correlation thresholds, the temporal baseline, the patch size for phase unwrapping, and other information concerning the processing history. The processing parameter files are first initialized with default values and then updated by the operator during the processing. Once optimal processing parameters for the individual SLC pairs are

¹The latest version of *3D_DISP.py* can be found on the the appended CD-ROM.

A.1. Automation of the processing chain

found, the script allows an easy exchange of input parameters, e.g. DEMs and GCPs. After a first run of *3D_DISP.py*, the directory structure is created as shown in Figure A.1 (third line). A folder has been created for every combination between two SLC images listed in the SLC list. These folders are named after the specific SLC images and additionally *1D_Master* or *1D_Slave*, representative for the generation of a descending or an ascending one-dimensional displacement field (Figure 4.1). Another folder is created for the three-dimensional combination of the one-dimensional velocity fields. At the same time shell scripts are created automatically for each folder. These subordinated shell scripts drive the GAMMA commands as well as other pre-written GAMMA shell scripts. All *1D folders* contain an *Insar.sh* script which executes the GAMMA commands for the interferogram generation (Chapter 4.1) and a *DISP.sh* script for the actual one-dimensional displacement map generation (master or slave). The adjustment with external GCPs (Chapter 4.4) is implemented in this script. The *3D folders* contain *DISP_3D.sh* shell scripts which drive the GAMMA tools for the combination of the specific one-dimensional velocity fields. The *Insar.sh* scripts have to be executed before the *DISP.sh* scripts which in turn have to be executed before the *DISP_3D.sh* script (Figure 4.1). Therefore, a *run_all.sh* script is written automatically by *DISP.py*, which executes the scripts in the respective folders in the correct sequence.

With this degree of automation, the latest version of the processing history is stored well-arranged in the processing parameter files. Also, other SLC image pairs can now easily be included via the *SLC_list* to increase spatial coverage. If new DEMs become available (e.g. TanDEM-X), the entire set of SLC images can in theory be reprocessed by changing the input DEM.

A.2. Velocity profiles

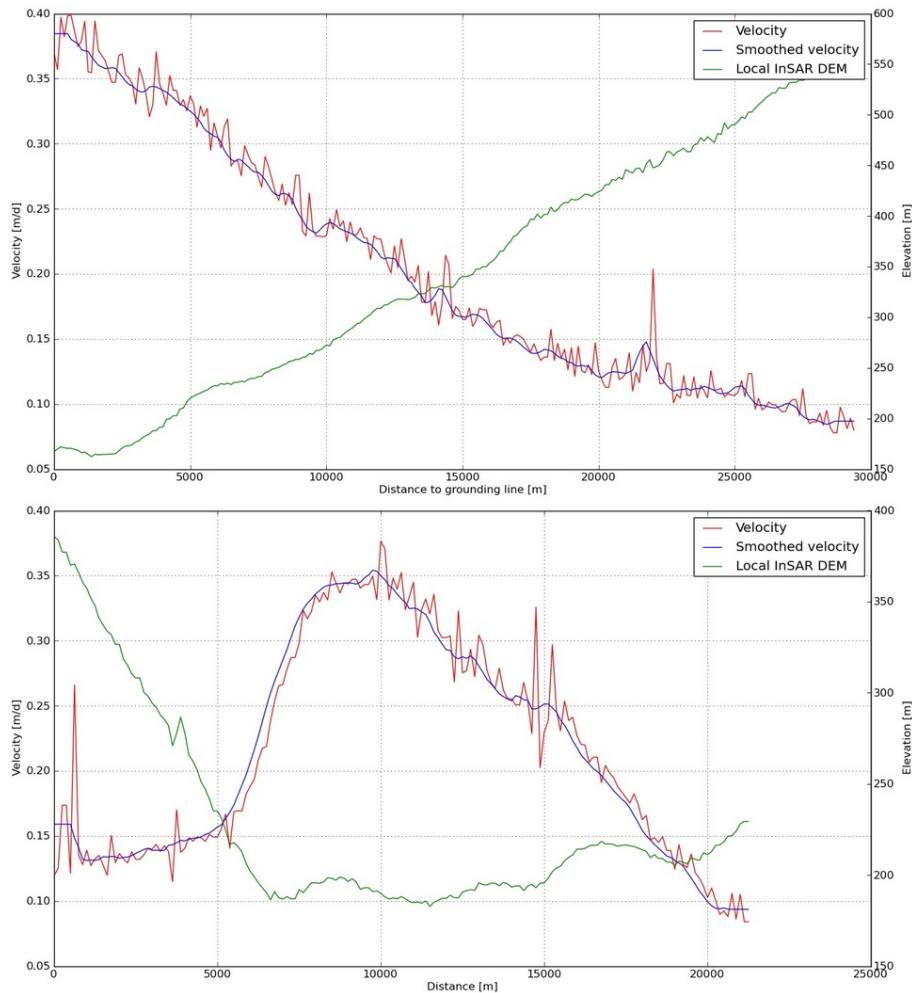


Figure A.2.: Top: Profile 1 as shown in Figure 5.7. Changes in ice flow are shown together with changes in elevation on a transect perpendicular to the grounding line. Bottom: Profile 3 as shown in Figure 5.7. The profile has been taken perpendicular to profile 1. One can see that the velocity of ice flow increases towards the center of the channeled ice stream.

A.2. Velocity profiles

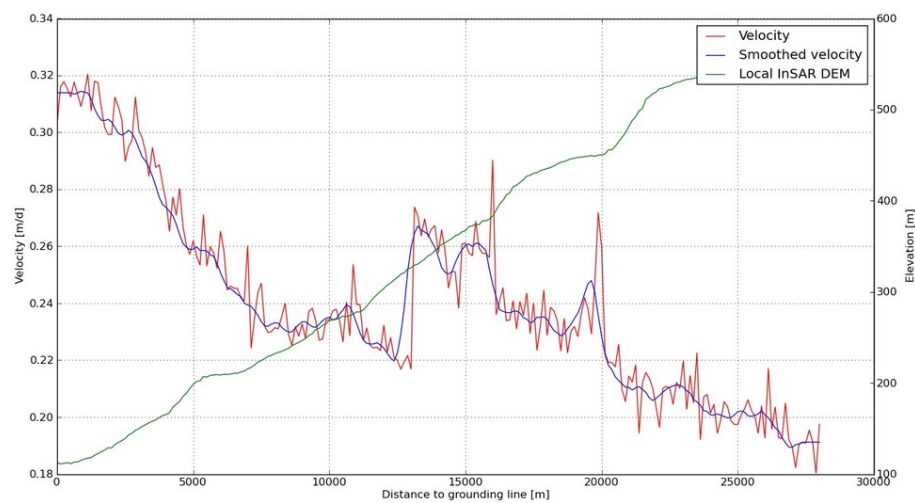


Figure A.3.: Profile 5 as shown in Figure 5.7. Changes in ice flow are shown together with changes in elevation on a transect perpendicular to the grounding line. A gap of ~ 0.05 m/d can be seen at a distance of about 13000 m from the grounding line. This gap originates from mosaicking of different three-dimensional velocity fields.

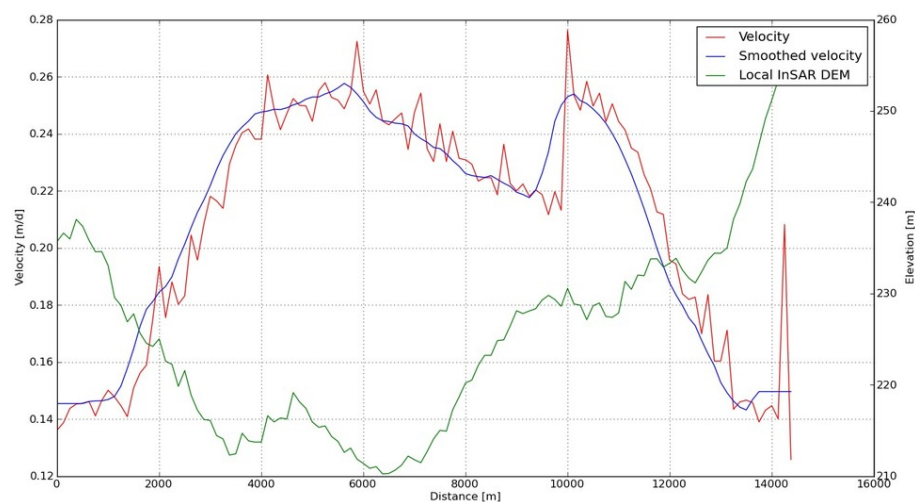


Figure A.4.: Profile 4 as shown in Figure 5.7. The profile is taken across the same ice stream as profile 5, therefore the mosaicking gap can be identified as well.

Acknowledgments

First and foremost, I want to thank my supervisor *Reinhard Drews* who helped me with a lot of patience and joking through this thesis. This thesis would not have been possible without his support, whether in Bremerhaven, Rottenburg or Christchurch.

My visit to New Zealand would not have been of such a great value without the support of *Wolfgang Rack* and his white board. Thank you Wolfgang. Also, climbing at the YMCA was one of my favorite activities. I decided to write this thesis in English, so that anybody interested could take a look on it. I want to thank the whole team from *Gateway Antarctica* for a great time. I felt comfortable right from the beginning.

On the German side, I want to thank the whole AWI glaciology and LIMPICS group. Working at AWI was enriching and gave me a good insight into glaciology. The good experience I had in Bremerhaven was not at least due to the very friendly work climate. In particular, I want to thank *Christine Wesche* for providing me with GPS measurements and *Veit Helm* for making the airborne laser altimetry data available.

I want to thank *PD Dr. Olaf Eisen* and *Prof. Dr. Lucas Menzel* for agreeing to correct my thesis and for always having a sympathetic ear. Especially, I want to thank Olaf for taking me to Antarctica.

I want to thank *Christine Beck* and *Robert Shoeman* for proofreading my thesis and providing me with very valuable hints, commas and English grammar.

Bibliography

- Albertz, J. (2007). *Einführung in die Fernerkundung. Grundlagen der Interpretation von Luft- und Satellitenbildern*. Wissenschaftliche Buchgesellschaft.
- ASTER GDEM Validation Team (2009). *ASTER Global DEM Validation*. METI, NASA, USGS.
- Bamber, J., Layberry, R., and Gogineni, S. (2001). A new ice thickness and bed data set for the Greenland ice sheet, 1. Measurement, data reduction, and errors. *Journal of Geophysical Research*, 106:33733–33780.
- Bamber, J. L., Gomez-Dans, J. L., and Griggs, J. A. (2009). A new 1km digital elevation model of the Antarctic derived from combined satellite radar and laser data – Part 1: Data and methods. *The Cryosphere*, 3:101–111.
- Bell, R. E. (2009). Rutschgefährdete Eisschilde. *Spektrum der Wissenschaft*, 4:32–39.
- Bentley, C. R. and Thomas, R. H. (2007). Global outlook for ice & snow - 6a ice sheets.
- Bindoff, N., Willebrand, J., Artale, V., Cazenave, A., Gregory, J., Gulev, S., Hanawa, K., Le Quéré, C., Levitus, S., Nojiri, Y., Shum, C., Talley, L., and Unnikrishnan, A. (2007). Observations: Oceanic Climate Change and Sea Level. In *Climate Change 2007: The Physical Science Basis. Contribution of Working Group I to the Fourth Assessment Report of the Intergovernmental Panel on Climate Change*. Cambridge University Press, Cambridge, United Kingdom and New York, NY, USA.
- Bindschadler, R. (2007). ASAILD – Antarctic Surface Accumulation and Ice Discharge. In *IPY Activity ID 88*.
- Chen, J. L., Wilson, C. R., D., B., and Tapley, B. D. (2009). Accelerated Antarctic ice loss from satellite gravity measurements. *Nature Geoscience*, 2:859–862.

Bibliography

- Cracknell, A. P. (2001). *Remote Sensing and Climate Change*. Springer.
- Cuffey, K. M. and Paterson, W. S. B. (2010). *The physics of glaciers*. Butterworth-Heinemann.
- Cumming, I. and Wong, F. (2005). *Digital processing of Synthetic Aperture Radar data*. Artech House.
- D'Elia, S. and Jutz, S. (1997). *SAR Mission Planning for ERS-1 and ERS-2*. ESA Bulletin Nr. 90.
- DLR (2010). TanDEM-X Science Home: TanDEM-X - A New High Resolution Interferometric SAR Mission.
- Drews, R., Rack, W., Wesche, C., and Helm, V. (2009). A spatially adjusted elevation model in Dronning Maud Land, Antarctica, based on differential SAR Interferometry. *IEEE Transactions on Geoscience and Remote Sensing*, 47:2501–2509.
- Dyck, S. and Peschke, G. (1995). *Grundlagen der Hydrologie*. Verl. für Bauwesen.
- Dyurgerov, M. and Meier, M. F. (2005). Glaciers and the Changing Earth System: A 2004 Snapshot. *Occasional Paper 58, Institute of Arctic and Alpine Research, University of Colorado, Boulder, CO*, 58:118.
- Eisen, O., Frezzotti, M., Genthon, C., Isaksson, E., Magand, O., van den Broeke, M. R., Dixon, D. A., Ekaykin, A., Holmlund, P., Kameda, T., Karlof, L., Kaspari, S., Lipenkov, V. Y., Oerter, H., Takahashi, S., and Vaughan, D. G. (2008). Ground-based measurements of spatial and temporal variability of snow accumulation in East Antarctica. *Reviews of Geophysics*, 46:1–39.
- Ferretti, A., Monti-Guarnieri, A., Prati, C., and Rocca, F. (2007). *InSAR Principles: Guidelines for SAR Interferometry Processing and Interpretation*. ESA.
- Fricker, H. A. and Padman, L. (2006). Ice shelf grounding zone structure from ICESat laser altimetry. *Geophysical Research Letters*, 33:1–5.
- Hambrey, M. and Alean, J. (2004). *Glaciers*. Cambridge Univ. Press.
- Helm, V., Rack, W., Cullen, R., Nienow, P., Mair, D., Parry, V., and Wingham, D. J. (2007). Winter accumulation in the percolation zone of Greenland measured by airborne radar altimeter. *Geophysical Research Letters*, 34:1–4.

- ITT (2002). *Envi 4.4 Manual*. ITT Visual Information Solutions.
- Joughin, I., Kwok, R., and Fahnestock, M. (1996). Estimation of ice-sheet motion using satellite radar interferometry: method and error analysis with application to Humboldt Glacier, Greenland. *Journal of Glaciology*, 42:564–575.
- Joughin, I. R., Kwok, R., and Fahnestock, M. A. (1998). Interferometric estimation of three-dimensional ice-flow using ascending and descending passes. *IEEE Transactions on Geoscience and Remote Sensing*, 36:25–37.
- Kwok, R. and Fahnestock, M. A. (1996). Ice sheet motion and topography from radar interferometry. *IEEE Transactions on Geoscience and Remote Sensing*, 34:189–200.
- Lemke, P., Ren, J., Alley, R., Allison, I., Carrasco, J., Flato, G., Fujii, Y., Kaser, G., Mote, P., Thomas, R., and Zhang, T. (2007). Observations: Changes in Snow, Ice and Frozen Ground. In *Climate Change 2007: The Physical Science Basis. Contribution of Working Group I to the Fourth Assessment Report of the Intergovernmental Panel on Climate Change*. Cambridge University Press, Cambridge, United Kingdom and New York, NY, USA.
- Liu, H., Zhao, Z., Yu, J., and Jezek, K. (2008). Simultaneous Least Squares Adjustment of Multiframe Velocities Derived From Interferometric and Speckle-Tracking Methods. *IEEE Geoscience and Remote Sensing Letters*, 5:289–293.
- Lythe, M. and Vaughan, D. (2001). A new ice thickness and subglacial topographic model of Antarctica. *Journal of Geophysical Research*, 106(B6):11335–11351.
- Massom, R. and Lubin, D. (2006). *Polar Remote Sensing. Volume II Ice Sheets*. Springer.
- Massonnet, D. and Feigl, K. L. (1998). Radar interferometry and its application to changes in the Earth’s surface. *Reviews of Geophysics*, 36:441–500.
- Meyer, F. J. (2004). *Simultane Schätzung von Topographie und Dynamik polarer Gletscher aus multi-temporalen SAR Interferogrammen*. PhD thesis, TU München.
- Mohr, J. J., Reeh, N., and Madsen, S. N. (1998). Three-dimensional glacial flow and surface elevation measured with radar interferometry. *Nature*, 391:273–276.
- Moll, A. (2008). *Radarinterferometrische Untersuchungen mit ERS-1/2 auf der An-*

Bibliography

- tarktischen Halbinsel*. PhD thesis, Rheinische Friedrich-Wilhelms-Universität Bonn.
- Neteler, M. and Mitasova, H. (2008). *Open Source GIS: A GRASS GIS Approach*. Springer.
- Rabus, B. T. and Lang, O. (2002). On the representation of ice-shelf grounding zones in SAR interferograms. *Journal of Glaciology*, 48:345–356.
- Rack, W., Doake, C. S. M., Rott, H., Siegel, A., and Skvarga, P. (2000). Interferometric analysis of the deformation pattern of the northern Larsen Ice Shelf, Antarctic Peninsula, compared to field measurements and numerical modeling. *Annals of Glaciology*, 31:205–210.
- Rahmstorf, S. and Schellnhuber, H.-J. (2007). *Der Klimawandel*. Beck.
- Riedel, B. (2002). *Modelle zur Beschreibung des gezeitenbedingten Bewegungsverhaltens von Schelfeisen in der Übergangszone*. PhD thesis, TU Braunschweig.
- Riedel, B., Nixdorf, U., Heinert, M., Eckstaller, A., and Mayer, C. (1999). The response of the Ekströmisen (Antarctica) grounding zone to tidal forcing. *Annals of Glaciology*, 29:239–242.
- Roland, N. W. (2009). *Antarktis. Forschung im ewigen Eis*. Spektrum Akademischer Verl.
- Rosen, P. A., Hensley, S., Joughin, I. R., Li, F. K., Madsen, S. N., Rordriguez, E., and Goldstein, R. M. (2000). Synthetic Aperture Radar Interferometry. *Proceedings of the IEEE*, 88:333–382.
- Rotschky, G., Holmlund, P., Isaksson, E., Mulvaney, R., Oerter, H., Van Den Broeke, M. R., and Winther, J.-G. (2007). A new surface accumulation map for western Dronning Maud Land, Antarctica, from interpolation of point measurements. *Journal of Glaciology*, 53:385–398.
- Rott, H., Müller, F., Nagler, T., and Floricioiu, D. (2010). The imbalance of glaciers after disintegration of Larsen B ice shelf, Antarctic Peninsula. *The Cryosphere Discussions*, 4:1607–1633.
- Rott, H., Rack, W., Skvarga, P., and De Angelis, H. (2002). Northern Larsen Ice Shelf, Antarctica: further retreat after collapse. *Annals of Glaciology*, 34:277–282.

- Sievers, J. and Bennat, H. (1989). Reference systems of maps and geographic information systems of Antarctica. *Antarctic Science*, 4:357–362.
- Sykes, H. J., Murray, T., and Luckmann, A. (2009). The location of the grounding zone of Evans Ice Stream, Antarctica, investigated using SAR interferometry and modelling. *Annals of Glaciology*, 50:35–40.
- Vaughan, D. G. (2009). Ice2sea – the future glacial contribution to sea-level rise. In *Geophysical Research Abstracts*, volume 11. EGU.
- Wegmüller, U. and Werner, C. (2002). *GAMMA reference manual*. Gamma Remote Sensing.
- Werner, C., Wegmüller, U., Strozzi, T., and Wiesmann, A. (2000). GAMMA SAR and Interferometric Processing Software. In *ERS - ENVISAT Symposium, Gothenburg, Sweden*.
- Wesche, C. (2009). *Evaluation and application of GPS and altimetry data over central Dronning Maud Land, Antarctica: annual elevation change, a digital elevation model and surface flow velocity*. PhD thesis, University of Bremen.
- Wesche, C., Riedel, S., and Steinhage, D. (2009). Precise surface topography of the grounded ice ridges at the Ekströmsisen, Antarctica, based on several geophysical data sets. *ISPRS Journal of Photogrammetry and Remote Sensing*, 64:381–386.
- Wilhelm, F. (1975). *Schnee- und Gletscherkunde*. de Gruyter.
- Winsborrow, M. C. M., Clark, C. D., and Stokes, C. R. (2010). What controls the location of ice streams? *Earth-Science Reviews*, 103:45–59.
- Zhang, T., Barry, R. G., Knowles, K., Heginbottom, J. A., and Brown, J. (1999). Statistics and characteristics of permafrost and ground-ice distribution in the Northern Hemisphere. *Polar Geography*, 23:132–154.
- Zhang, T., Barry, R. G., Knowles, K., Ling, F., and Armstrong, R. L. (2003). Distribution of seasonally and perennially frozen ground in the Northern Hemisphere. In *Proceedings of the 8th International Conference on Permafrost, 21-25 July 2003, Zürich, Switzerland*.